Visualizing the DNA repair process by a photolyase at atomic resolution

Manuel Maestre-Reyna, Po-Hsun Wang, Eriko Nango, Yuhei Hosokawa, Martin Saft, Antonia Furrer, Cheng-Han Yang, Eka Putra Gusti Ngurah Putu, Wen-Jin Wu, Hans-Joachim Emmerich, et al.

Watching the entire DNA repair process by a photolyase at atomic resolution in real time

Manuel Maestre-Reyna[1,2,*], Po-Hsun Wang[1], Eriko Nango[3,4], Yuhei Hosokawa[5], Martin Saft[6], Antonia Furrer[7], Cheng-Han Yang[1], Eka Putra Gusti Ngurah Putu[1], Wen-Jin Wu[1], Hans-Joachim Emmerich[6], Nicolas Caramello[8,9], Sophie Franz-Badur[6], Chao Yang[10], Sylvain Engilberge[8,11], Maximilian Wranik[7], Hannah Louise Glover[7], Tobias Weinert[7], Hsiang-Yi Wu[1], Cheng-Chung Lee[1], Wei-Cheng Huang[1], Kai-Fa Huang[1], Yao-Kai Chang[1], Jiahn-Haur Liao[1], Jui-Hung Weng[1], Wael Gad[1], Chiung-Wen Chang[1], Allan H. Pang[1], Kai-Chun Yang[2], Wei-Ting Lin[2], Yu-Chen Chang[2], Dardan Gashi[7], Emma Beale[7], Dmitry Ozerov[7], Karol Nass[7], Gregor Knopp[7], Philip J. M. Johnson[7], Claudio Cirelli[7], Chris Milne[7], Camila Bacellar[7], Michihiro Sugahara[3], Shigeki Owada[3,12], Yasumasa Joti[3,12], Ayumi Yamashita[3,13], Rie Tanaka[3,13], Tomoyuki Tanaka[3,13], Fangjia Luo[12], Kensuke Tono[3,12], Wiktoria Zarzycka[14], Pavel Müller[14], Maisa Alkheder Alahmad[6], Filip Bezold[6], Valerie Fuchs[6], Petra Gnau[6], Stephan Kiontke[6], Lukas Korf[6], Viktoria Reithofer[6], Christian Joshua Rosner[6], Elisa Marie Seiler[6], Mohammed Watad[6], Laura Werel[6], Roberta Spadaccini[6,15], Junpei Yamamoto[5], So Iwata[3,13], Dongping Zhong[16], Joerg Standfuss[7], Antoine Royant[8,11], Yoshitaka Bessho[1,3,17,*], Lars-Oliver Essen[6,*], Ming-Daw Tsai[1,18,*]

[1]Institute of Biological Chemistry, Academia Sinica, 128 Academia Rd. Sec. 2, Nankang, Taipei, 115, Taiwan.
[2]Department of Chemistry, National Taiwan University, 1, Roosevelt Rd. Sec. 4, Taipei 106, Taiwan.
[3]RIKEN SPring-8 Center, 1-1-1 Kouto, Sayo, Hyogo, 679-5148, Japan.
[4]Institute of Multidisciplinary Research for Advanced Materials, Tohoku University, 2-1-1 Katahira, Aoba-ku, Sendai 980-8577, Japan
[5]Division of Chemistry, Graduate School of Engineering Science, Osaka University, 1-3 Machikaneyama, Toyonaka, Osaka 560-8531, Japan.
[6]Department of Chemistry, Philipps University Marburg, Hans-Meerwein Strasse 4, Marburg 35032, Germany.
[7]Paul Scherrer Institute, Forschungstrasse 111, 5232 Villigen PSI, Switzerland
[8]European Synchrotron Radiation Facility, 38043 Grenoble, France.
[9]Hamburg Centre for Ultrafast Imaging, Universität Hamburg, 22761 Hamburg, Germany
[10]Department of Physics, Ohio State University, Columbus, Ohio State University, 43210
[11]Univ. Grenoble Alpes, CNRS, CEA, Institut de Biologie Structurale (IBS), 38044 Grenoble, France.
[12]Japan Synchrotron Radiation Research Institute, 1-1-1 Kouto, Sayo, Hyogo, 679-5198, Japan.
[13]Department of Cell Biology, Graduate School of Medicine, Kyoto University, Yoshidakonoe-cho, Sakyo-ku, Kyoto, 606-8501, Japan.
[14]Université Paris-Saclay, CEA, CNRS, Institute for Integrative Biology of the Cell (I2BC), 91198 Gif-sur-Yvette, France.

[15]Dipartamento di Scienze e tecnologie, Universita degli studi del Sannio, Benevento, Italy.
[16]Department of Physics, Department of Chemistry and Biochemistry, Programs of Biophysics and Chemical Physics and Biochemistry, The Ohio State University, Columbus, Ohio 43210.
[17]Graduate School of Agricultural and Life Sciences, The University of Tokyo, 1-1-1 Yayoi, Bunkyo, Tokyo 113-8657, Japan.
[18]Institute of Biochemical Sciences, National Taiwan University, 1, Roosevelt Rd. Sec. 4, Taipei 106, Taiwan.

*Corresponding authors. Email: mmaestre@ntu.edu.tw (M.M.R.); bessho@g.ecc.u-tokyo.ac.jp (Y.B.); essen@chemie.uni-marburg.de (L.O.E.); mdtsai@gate.sinica.edu.tw (M.D.T.)

Abstract

Photolyases, a ubiquitous class of flavoproteins, are light-dependent enzymes that employ blue light to repair DNA photolesions. Here, we determined the structural mechanism of photolyase-catalyzed repair of a cyclobutane pyrimidine dimer (CPD) lesion at atomic and picosecond resolutions via time-resolved serial femtosecond X-ray crystallography (TR-SFX). We obtained 18 snapshots at different time points, whose predominantly accumulated structures were solved by structure factor extrapolation followed by structural refinement. As this light-triggered process involving electron transfer to the CPD lesion required a high laser power for achieving reasonable repair efficiencies, we carefully addressed and discussed potential multiphoton effects. Each structural snapshot is assignable to elementary steps of the catalytic cycle given time-dependent changes in four reaction loci and corroborating data from complementary methods. The resulting 3D movie depicts first the repair of CPD lesions in the pico- to nanosecond range and how it is orchestrated by conformational changes of the catalytic flavin and other active site moieties. During the first nanoseconds, intermediate structures show the steps of forward electron transfer between the coenzyme $FADH^-$ and the CPD lesion, bond breaking, ring opening, and back electron transfer. These chemical steps are followed by recovery of the enzymatic moieties involved in catalysis, forming the fully reduced enzyme-product complex at 500 nanoseconds. Finally, during product release, back-flip intermediates of the thymine bases to reanneal the dsDNA were captured at 25-200 microseconds. Our data cover now the complete molecular mechanism of one of the most widespread DNA repair mechanisms, and importantly, its chemistry and enzymatic catalysis at work in real time and at atomic resolution.

The last 5-10 years have seen major breakthroughs in the determination and analysis of macromolecular structures, contributed by two powerful techniques, cryo-electron microscopy (cryo-EM) and time-resolved serial femtosecond crystallography (TR-SFX) using X-ray free electron lasers (XFEL). While the major advantage of cryo-EM is its capability to solve large complexes (*1*, *2*), TR-SFX enabled the monitoring of light-induced structural changes of macromolecules in real time (*3–5*). So far, the majority of TR-SFX studies addressed *trans-cis* isomerization and resulting conformational changes in photoreceptors (*6–10*) or ion pumps (*11*, *12*), and the redox mechanism of photosystems (*13–17*). Only recently several TR-SFX reports have started to analyze the structural mechanisms of enzymatic catalysis (*16–21*).

Photolyases catalyze the repair of damaged DNA containing UV-induced lesions, including cyclobutane pyrimidine dimers (CPD) and the 6-4 photoproduct (6-4PP) (*22*, *23*). CPD lesions are the most abundant in nature upon UVB exposure and the major cause for skin cancer in humans (*24*). Catalysis by CPD photolyases involves multiple redox reactions and a multi-step splitting of the cyclobutane ring (*25*). The enzyme is first activated via photoreduction of its coenzyme flavin adenine dinucleotide (FAD) from the oxidized (FAD_{ox}) to the reduced state ($FADH^-$) (*26*). This process requires two single-electron transfer steps mediated by an electron transfer chain involving three tryptophan residues, yielding respectively the radical semiquinone intermediate ($FAD^{\bullet-}$ or its protonated form $FADH^{\bullet}$) and the reduced, anionic hydroquinone state ($FADH^-$) (*27*). Only the latter is capable of catalyzing light-induced DNA repair. The mechanisms of photoreduction and DNA repair have been elucidated by extensive spectroscopic and theoretical studies over the past three decades (*22*, *26*, *28–32*). However, relatively limited information from high-resolution crystal structures is available, and, except from apo-forms (*33–35*), all such structures were obtained using synchrotron X-ray radiation that induced both photoreduction (*36–38*) and DNA repair reactions (*39*).

Recently, we employed TR-SFX to elucidate the structural mechanism of the photoreduction processes in the *Methanosarcina mazei* class II CPD photolyase (*Mm*CPDII) (*33*). We identified an Asn/Arg-Asp redox sensor triad that regulates FAD re-hybridization and protonation, and observed buckling and twisting of the isoalloxazine ring of the coenzyme FAD, which occurred in the submicrosecond regime after the light-triggered electron transfer step. The TR-SFX study of the photoreduction process has set the stage to study the main function of the *Mm*CPDII photolyase, the now presented repair of CPD lesions.

On the basis of extensive spectroscopic and computational analyses (*22*, *23*, *25*, *26*, *40*, *41*), the repair of the cyclobutane-bridged TT dimer (T<>T, **1** in **Fig. 1A**) by photolyases was suggested to go through three intermediates. First, a forward electron transfer (forward ET or FET) from the reduced coenzyme $FADH^-$ produces $(T<>T)^{\bullet -}$ (**2**), where the excess electron may be delocalized between the two pyrimidines. The resulting CPD radical anion undergoes then cleavage of its C5-C5' bond to produce $(T\_T)^{\bullet -}$ (**3**) and further cleavage of the C6-C6' bond to give $(T+T)^{\bullet -}$ (**4**). The latter then transfers an electron back to the flavin coenzyme to produce the repaired thymines (T+T, product, designated as **5** in **Fig. 1A**). While such a repair mechanism is chemically feasible and well supported by spectroscopic data, structures of its reaction intermediates await elucidation in the enzyme bound form. Furthermore, given the moderate quantum yields for DNA repair, at least in class II photolyases, the underlying interactions between reaction intermediates, the isoalloxazine ring of the coenzyme and active site residues of the photolyase, remain to be probed by high-resolution data. The first goal of this TR-SFX study was hence to identify and characterize five reaction intermediates corresponding to the chemical intermediates of **Fig. 1A** in the DNA-enzyme complex, **Int1 to Int5.** Their assignment was based on observed changes of the coenzyme's geometry, conformations of active site residues and the chemical state of the CPD during its repair.

When complexed to photolyases, the TT dimer in UV-damaged DNA, which retains base pairing with adenine counterbases in the unbound state, though somewhat twisted (*42*), flips out of double-stranded DNA (dDNA) to interact with the FAD coenzyme and active site residues. This double-flip causes a strong kink in the canonical B-DNA structure, and creates an unpaired bubble that is stabilized by the photolyase's bubble-intruding region (BIR) (*43*). Accordingly, a second goal of this TR-SFX study was to identify the conformational intermediates (**Con**), which correspond to the inverse conformational changes required for dsDNA reannealing and dissolution of the DNA-photolyase complex after completion of the chemical CPD repair. As photolyases bind regular, i.e. already repaired, dsDNA >4 orders of magnitude weaker than UV-damaged dsDNA (*44*), this analysis may be particularly rewarding given that spectroscopic signatures of thymine bases are essentially identical before and after flip-back so that very little dynamic information is available for the late part of the reaction cycle.

Results

Tailoring TR-SFX for uncovering the photolyase mechanism

Our DNA repair study depended on co-crystals of fully reduced *Mm*CPDII (*32*) and CPD-containing DNA (**Fig. 1B**) (*43*), which were grown within 12 h prior to use directly at XFEL sites using anaerobic tents and safety light conditions. Two sets of TR-SFX data were collected: One covers the CPD repair reaction itself from 100 ps to 10 ns (the ps-ns series) as performed at SwissFEL, where crystals were excited via a 0.98 ps long, 10 µJ, 400 nm pump laser pulse with a 50 µm diameter focal spot. For the second time series that covers relaxation of the photolyase-product complex and DNA release (10 ns - 200 µs, the ns-µs series, SACLA), samples were excited via a 3 ns long, 150 µJ, 408 nm pump laser pulse with a 100 µm focal spot diameter. Although illumination at ~400 nm likely generates a mixture of S1 and S2 excited $FADH^{-*}$ species, the S2→S1 decay has been noted to occur within a few ps, considerably faster than FET (*45*).

For photolyase-mediated DNA repair TR-SFX conditions were optimized for achieving anticipated DNA repair yields, as detailed in **Supplementary Text S1** and **figs. S1, S2**. A brief summary is provided here: (i) We confirmed that the oxidized form of *Mm*CPDII, was unable to initiate FET towards CPD and failed to cause any effects including repair of the CPD under very high laser powers, both under ps-ns and ns-µs conditions (**figs. S1A, B**). (ii) Prior to TR-SFX experiments addressing CPD repair itself, we validated that difference density signatures of the 10 ns TR-SFX structure (**fig. S1E**) coincided with that initially reported from X-ray radiation-triggered repair (**fig. S1C**) (*38*, *39*) and low-dosage LED-induced repair (**fig. S1D**). (iii) Reduction of laser power from 10 µJ to 5 µJ in the ps-ns series caused diminished signature signals (**fig. S2B**). (iv) Control experiments for light contamination assured clean dark datasets (**figs. S2A, B**).

In TR-SFX experiments the power and energies of laser excitation pulses generally exceed one absorbed photon per chromophore thus implying potential multiphoton effects in light-triggered systems, which may affect the photochemical reaction course and dynamics (*46–51*). We found that not more than ~68 % of incident light is accessible for microcrystals embedded in grease due to light scattering (**Supplementary Text S2** and **fig. S3**). Accordingly, calculation of photon dosages as absorbed by the enzyme have to take this and other factors like the quantum yields into account. Nevertheless, our results indicated that up to 10 and 30 photons are potentially absorbed

per FAD chromophore per pulse for the ps-ns and the ns-µs series, respectively (**Supplementary Text S3**), which are high enough to cause activation of the $FADH^-$ coenzyme to levels higher than the S1 state. However, electronic relaxation of $FADH^{-}$* to S1 from higher states than S2 is expected to proceed even faster than the S2→S1 transition by internal conversion (*45*), i.e. in the sub-ps range. Given the time-resolution of our TR-SFX experiments (**Table 1**), multiply excited $FADH^-$ species should have been decayed prior to the first catalytic event, i.e. electron-transfer to the CPD lesion.

Analyzing TR-SFX data for photolyase-mediated CPD-DNA repair

Given the complex set of TR-SFX data a brief explanation of methods for structural analysis and nomenclature is given first. For structure factor extrapolation and refinement, we followed previously described guidelines (*5*, *9*, *52*, *53*). For both time-series, the basic conditions and main structural features are summarized in **Table 1**, while the detailed structural parameters are listed in **tables S1 and S2**. Each structure is given a name in column 1 of **Table 1**, e.g. F10ns and N10ns for the 10 ns snapshots, where the one letter code indicates the type of pumping laser (F for femtosecond laser pump in the ps-ns series, and N for nanosecond pump in the ns-µs series), followed by the delay time after illumination (with "dark" designating a non-illuminated time-resolved control structure). Exceptions are the steady-state structures in the oxidized (ox/ss) and fully reduced states (Fdark, Ndark). Isomorphous difference electron density maps (ΔFo) (*54*) were calculated to decipher structural differences, which are designated as difference between two states, ΔFo(Y-X).

Major properties of each structural snapshot are depicted in columns 3-11 of **Table 1**, which include features from the four main reaction loci (**Fig. 2**). These properties are considered in the interpretation of each structural snapshot. For the ps-ns series the focus was on CPD repair. The structural snapshots were hence assigned to match the TT status of the proposed intermediates **1-5** (**Fig. 1A**), and designated as **Int1-Int5** of the photolyase-DNA complexes (**Table 1**). For the ns-µs series with its already completed CPD repair reaction, structural snapshots reflecting post-repair reactions are designated as conformational intermediates (**Con1-Con4**), with close variants being further subdivided by a, b, ...

Structural analysis of the TR-SFX data was conducted in three rounds: First, on the basis of mainly structural changes at CPD and $FADH^-$ (two of the four reaction loci, **Fig. 2**), each time-

point was assigned intermediates playing a role in the catalytic cycle. Next, structural changes in the other two reaction loci were included to fine-tune the interpretation of each time point. Finally, all datasets and interpretations were considered together along with additional supporting evidence derived from electron density analyses, singular value decomposition (SVD), and quantum mechanical (QM) calculations.

The four main reaction loci of CPD-DNA repair by *Mm*CPDII

Global structures of the *Mm*CPDII-DNA complex as determined via SFX in both the oxidized and fully reduced states (ox/ss, Fdark., **Fig. 2A**, and Ndark) agree well with prior synchrotron structures of the DNA complex in the oxidized states (*37*, *43*) and *Mm*CPDII SFX structures without bound DNA in all redox states (*33*). However, difference density peaks are found at four main loci: the CPD structure (**Fig. 2B**), the FAD coenzyme (**Fig. 2C**), the active site moieties R256 and 5WC (**Fig. 2D**), and the class II photolyase-defining BIR (**Fig. 2E**). These loci show also all prominent difference density map features after light-triggered DNA repair, though the general protein fold itself is not affected (**fig. S4**). In this section, we survey the four main reaction loci and explain how the relevant data in **Table 1** were obtained.

(1) CPD locus: To track CPD repair itself, we used two key indicators based on the characteristic CPD difference density features. First, we determined the C5-C5’ and C6-C6’ peak-to-peak distances (designated as C-C peak distances) between the maxima of the difference map peaks along the axes of the C5-C5’ and C6-C6’ bonds (**Table 1**, column 8 and footnote c, **Materials and methods summary, fig. S5**). Secondly, we calculated the average integrated negative electron densities (designated as negative densities) from difference maps around C5 and C6 atoms as a function of time (**Table 1**, column 9 and footnote e, **Supplementary Text S4,** and **fig. S13B**), which is a good indicator of the accumulation of repair intermediates where the corresponding bond had been broken.

(2) FAD locus: Subtle redox-dependent changes around the flavin site, including increased buckling of the FAD upon reduction (**Fig. 2C**), is consistent with our recent studies of *Mm*CPDII photoreduction (*33*). There, we showed by monitoring ρ_C and ρ_N dihedral angles (**Fig. 1C**) that the isoalloxazine ring of the FAD coenzyme undergoes a sequence of buckling and twisting motions during the process of photoreduction and protonation. In the oxidized state FAD_{ox}, the isoalloxazine moiety was only very mildly buckled (ρ_C, ρ_N: 2.0°, 2.0°), whereas in the catalytic

FADH$^-$ state, the isoalloxazine moiety was strongly buckled (ρ_C, ρ_N: 14.3°, 14.5°). In the semiquinone FADH$^\bullet$ state, it moved closer to planarity (ρ_C, ρ_N: 4.6°, 4.8°) (*33*). Since FADH$^-$ is transiently oxidized into FADH$^\bullet$ upon forward ET toward CPD, then recovered upon reaction completion, the ρ_C and ρ_N dihedral angles may hence well reflect the electron flow during CPD repair (**Table 1**, columns 4 and 5).

(3) 5WC/R256 locus. In the active site, the substrate interacts with several key features of the enzyme (**Fig. 2D**), including the adenine moiety of FAD, the highly conserved residue R256, and the structurally conserved five-water cluster. In the fully reduced state, i.e. Fdark and Ndark, the 5WC bridges the bisphosphate backbone of FAD and R256 so that it contributes to the electrostatic stabilization of the anionic FADH$^-$. Upon FET, R256 moves to stabilize the CPD radical anion and the 5WC becomes disordered or dynamic. Changes in 5WC/R256 during repair are monitored in **Table 1** (column 6 and footnote f).

(4) BIR locus: In the bubble-intruding region (**Fig. 2E**), the D428/W431/R441 triad acts as a lock, both stabilizing the unpaired bubble, and firmly maintaining the protein-DNA complex (*43*), while R429 is more flexible, and capable of dynamically interacting with both CPD complementary bases, dA7' and dA8'. Here, post-repair base flip-back induced opening of the BIR lock, as shown in **Table 1** (column 7 and footnote g).

Given our structural snapshots the entire process of photolyase-mediated repair of dsDNA can be assigned to three periods, i.e. early, middle, and late events, which correspond to CPD repair, active site recovery, and thymine back flip-DNA release, respectively. The loci of CPD structure and FAD geometry will be considered first to assess the primary repair process. The remaining two reaction loci will be then separately addressed. Taken together the results are then used to assemble a molecular movie covering DNA repair and ordered product release by photolyases.

Early events: Electron transfer-driven repair of the CPD lesion

The refined structures and difference maps from the ps-ns series monitor both the ring-opening steps of the CPD repair reaction and the concomitant FAD isoalloxazine moiety dynamics (**Fig. 3A**). The C5-C5' and C6-C6' peak distances as well as the integrated negative electron densitites (**Fig. 3B**) and the flavin dihedral angles ρ_C, ρ_N (**Fig. 3C**) are plotted over time. The structure of each time point in Figure 3A represents the predominantly accumulated species of a snapshot

during CPD repair. Although the structural changes shown here are subtle, the ΔFc(Y–dark) of each individual structure is always maximally correlated to its corresponding ΔFo(Y–dark) (**figs. S5A, S5B**), supporting the reliability and significance of the refined structural changes, and yielding a clear view of the process of DNA repair.

Accordingly, we have observed all proposed CPD repair intermediates **1** to **5** (**Fig. 1A)** in the enzyme bound form as **Int1/Int1*** to **Int5** (**Table 1**), where the Fdark structure represents **Int1** (T<>T/FADH^{-}). At 650 ps, the magnitude of the negative density feature around the C5-C5' bond is much higher than around the C6-C6' bond. In good agreement, the C5-C5' peak distance is 1.9 Å (**Figs. 3A, B** and **Table 1**) implying a broken C5-C5' and an intact C6-C6' bond, suggesting that the CPD ring-opening intermediate (T_T)$^{\bullet-}$, **Int3**, is dominant in the F650ps snapshot. At F1ns, with the negative density around C5-C5' being strong and that around C6-C6' growing, both C5-C5' and C6-C6' difference density peak distances reach 1.9 Å. Here, the dominant species corresponds to the repaired CPD intermediate (T+T)$^{\bullet-}$, **Int4**. Interestingly, these trends continue to the F2ns snapshot, suggesting a continuing build-up of **Int4**. This in turn suggests that F1ns may still contains a contribution by **Int3**.

The first structure after photon absorbtion corresponds to the activated coenzyme, FADH^{-*}. The F100ps snapshot (**Fig. 3A**) might represent this state since its CPD structure is unaltered while its isoalloxazine ring has greatly changed. Nevertheless, the R256 side chain has moved toward CPD, suggesting that FET from FADH^{-*} has already onset at this point. In the F250ps snapshot, the isoalloxazine ring continued to swing, as shown by sign-changes of its ρ_C and ρ_N angles (**Fig. 3C**). Although the CPD structure remains still unchanged, the nearby active site moieties R256/5WC have already onset to move as described later. These changes suggest that FET is in progress during both F100ps and F250ps snapshots, which represent a mixture of species, T<>T/FADH^{-*} (**Int1***) and (T<>T)$^{\bullet-}$/FADH$^{\bullet}$ (**Int2**). This ET-dependent reorganisation is in good agreement with such ultrafast redox transitions being stabilized via rapid isoalloxazine fluttering (*55*), and harmonic motions of other light-gathering cofactors after absorption (*49*).

In the F450ps snapshot, a C5-C5' peak distance could be measured for the first time as C5-C5' negative density has accumulated. Nevertheless, in the refined structure both the C5-C5' and C6-C6' bonds remained intact. This snapshot can be hence assigned to an **Int2/3** mixture, where Int2 is the major species. Interestingly, from F450ps and up to F1ns, structures showed relatively

planar FAD isoalloxazine geometries compared to the dark, fully reduced state (**Fig**. 3C), which is expected for the semiquinoid $FADH^{\bullet}$ form (*33*). This indicates that FET is mostly finished in the F450ps snapshot, and that the radical anionic CPD species dominate these snapshots. However, immediately after the 1 ns delay (at 2 ns and 3.35 ns), there are remarkable oscillatory motions of the FAD's isoalloxazine ring as indicated by ρ_C and ρ_N dihedral angles, which correlate well with fluttering that is associated with rapid relaxation after sudden redox changes (*22*). This fluttering suggests back electron transfer (BET) from the thymine radical anion to the coenzyme and is in good agreement with a BET time constant of ~700 ps according to time-resolved spectroscopic studies of CPD repair by photolyases (*56, 57*). Accordingly, we assign the F2ns and F3.35ns snapshots as representatives for the BET reaction, which should contain varying mixtures of $(T+T)^{\bullet-}/FADH^{\bullet}$ (**Int4**) and $(T+T)/FADH^{-}$ (**Int5**). In the F6ns snapshot, the isoalloxazine oscillatory motion appears to have receded, and therefore we propose that F6ns consists predominantly of the product after completion of the CPD repair, **Int5**. Since the structural properties of the next snapshot F10ns are very similar to F6ns (**Fig. 3A** and **Table 1**), F10ns represents further accumulation of the **Int5** product.

Middle events: base stacking and FAD site recovery

The ns-µs series of TR-SFX data addresses conformational changes of the repaired thymines and enzymatic moieties during product release. Throughout this series, the status of the intact thymines (T+T) and the coenzyme $FADH^{-}$ corresponds chemically to **Int5**. Nevertheless, given that the T+T and $FADH^{-}$ conformations and active site arrangements also differ in detail besides later conformational changes of the photolyase-product complex, we describe them as distinct conformational intermediates. Notably, the N10ns snapshot (**Con1**, first structure in **Fig. 4A**) and the F6ns/F10ns snapshots (**Int5**, **Fig. 3A**) coincide closely thus providing further evidence for the adequacy of experimental parameters used in both series. To our surprise, before onset of product release, the intact thymines stay fully stacked in the active site for up to 500 ns (**Table 1**, **Fig. 4A**). Apparently, the active site undergoes relaxation before the two repaired thymine bases start to flip back out of the active site. In the N100ns and N500ns snapshots, the isoalloxazine geometry of the $FADH^{-}$ coenzyme returns to the initial fully reduced state (**Fig. 4A**, **4C**). These two structures, assigned as **Con2a** and **Con2b** intermediates, respectively, differ only slightly for the 5WC/R256

316 locus (see below). Interestingly during photoreduction of *Mm*CPDII without bound DNA, the
317 isoalloxazine ring adopts similarly its full buckling at about 300 ns after its light-driven $FADH^{\bullet}$
318 → $FADH^{-}$ transition (*33*).

319 An interesting observation from these data is the rapid decrease of isoalloxazine dihedral
320 angles during FET, but slow increase and recovery after BET (**Fig. 3C**, **Table 1**). A possible
321 explanation is that FET occurs between CPD and the light-excited $FADH^{-*}$, with a singlet S_1 shell
322 occupying electron being transferred (*58*). The oxidation of $FADH^{-*}$ into $FADH^{\bullet}$ is a downhill
323 transition between an unstable, high-energy state to a stable low-energy state, whereas reduction
324 of $FADH^{\bullet}$ to $FADH^{-}$ represents a transition between two ground states (D_0 to S_0). Although BET
325 transiently perturbs the FADH structure, as evidenced by strong torsion and fluttering between 1
326 and 3 ns (**Fig. 3C**), the accumulated energy within the isoalloxazine moiety is only slowly
327 dispersed over hundreds of nanoseconds, as seen both here and previously for the *Mm*CPDII
328 photoreduction (*33*).
329
330
331 **Late events: base back-flip and onset of reannealing of double-stranded DNA**
332 The isoalloxazine geometry no longer changes in the 25 µs and 200 µs snapshots (**Fig. 4D**). Here,
333 the repaired thymine bases finally move out of the active site and flip back towards the dsDNA.
334 In continuation from prior time-points, where post-repair movement concentrated around the 5'-
335 thymine (**Figs. 3A, 4A**), it is the 5'-thymine (dT7) that first starts to exit the active site during the
336 N25µs snapshot. However, this back-flipping base is too disordered to be refined as only the
337 pentose is well resolved (**Fig. 4D**). Since the two thymine bases are no longer stacked and 5'-T
338 flips back, this structure can be considered as a "thymine back-flipping intermediate" (**Con3a**, TT
339 status: T/T). Meanwhile, the 3'-thymine dT8 is tilted in such a way that it occupies the full space
340 within the active site (**Fig. 4D**). The N200µs snapshot is particularly interesting, since the two
341 thymine bases continued the back-flipping process, but were captured at different stages in the two
342 complexes in the asymmetric unit. In complex A, the dT7 has further moved and its density has
343 now become well defined (intermediate **Con3b**, TT status: T/T). In complex B, both thymine bases
344 have flipped back and undergo base-pairing with their respective complementary bases. This
345 complex can be designated as the "product-reannealing complex" (**Con4)**, and its TT status (-T-
346 T-) corresponds to regular double-stranded DNA. Notably, there are extra difference signals in

complex A, which are fittable to **Con4** (30 to 50%), and likewise in complex B that correspond to **Con3b** (30 to 40%) (**fig. S7**). This population shift between complexes A and B in the N200µs snapshot likely derives from crucial crystal contacts made by complex A, but not complex B (**fig. S8**). In terms of thymine back-flipping, complex B is hence less constrained by the crystal lattice and can restore the integrity of the duplex DNA in a shorter timeframe. Considering that repaired dsDNA is known to dissociate from the photolyase (*36*, *43*), it is reasonable to consider **Con4** as a transient intermediate captured just prior to final complex dissociation. Unlike all structures up to 500 ns that show only few difference density peaks in the DNA region (**Fig. 4E**, left), the N200µs complex B reveals extensive difference density features along the entire dsDNA (**Fig. 4E** right).

Overall, the presented timeline outlines all chemical and structural changes undergone by the substrate CPD-DNA and the coenzyme FAD during the *Mm*CPDII reaction cycle. Next, the crucial contribution of the enzyme itself will be analyzed, providing a detailed mechanistic description of *Mm*CPDII reactivity, including additional support for our assignment of structural intermediates.

Active site dynamics during CPD repair: The 5WC/R256 locus

Concomitant to the reaction course of CPD repair as outlined before, further ΔFo peaks nearby hint at conformational changes in two highly conserved features of the class II photolyase active site, the 5WC and the side chain of R256 (**Fig. 2D**). Only in the catalytically active fully reduced (**Int1**) but not the oxidized state (ox/ss), the 5WC interacts with one of the Nη atoms of R256 to form a square bipyramidal structure that connects the FAD phosphate backbone, the CPD 3'-thymine and R256 (**Fig. 2D**). Upon reaction initiation, i.e. at 100 ps, R256 quickly retracts from the 5WC towards the CPD, with the side chain being still mobile and showing two alternative conformations (**Fig. 5A**). During the further reaction, the 5WC loses its order while the R256-CPD interaction persists, as shown for **Int3** of the F650ps snapshot as an example (**Fig. 5B**). Based on these structures and the corresponding structures of all time points (**fig. S9**), we suggest that the 5WC/R256 locus allows fast reorganization during the electron transfer reaction. In the resting, i.e. fully reduced state, 5WC/R256 electrostatically stabilizes the negatively charged $FADH^-$. Upon FET, R256 preferably stabilizes electrostatically the $CPD^{\bullet-}$ anion radical rather than the $FADH^\bullet$ radical, and destabilizes the ordered 5WC. In support of this hypothesis, the 5WC could not be found in either the ox/ss (**Fig. 2D**) or in any of the room temperature apo-structures of *Mm*CPDII

(**fig. S10**) (*33*), indicating that for the formation of a square bipyramidal structure of 5WC, anionic FAD and a bound CPD substrate are necessary. In *Mm*CPDII-CPD-DNA complexes obtained under cryogenic conditions at the synchrotron, a highly similar six-water cluster (6WC), in which the sixth water replaces R256, can be observed (*37, 43*) (**fig. S10**). Given that such a 6WC transiently appears during the BET, i.e. in the F3.35ns snapshot (**fig. S9)**, we propose that, for the synchrotron structures, the 6WC mimics an intermediate derived either from cryo-trapping or X-ray induced ET.

Our results on the electrostatic stabilization of the CPD radical anion by R256 are corroborated by previous mutational analysis (*56*, *59*). These studies showed that the corresponding R342A mutation in *Ec*CPDI caused impaired binding for photodamaged DNA and a diminished quantum yield for CPD repair (*56*). Accordingly, the 5WC/R256 locus of class II photolyases may act as a fail-safe device for $FADH^-$, priming it for FET activity only in the presence of a bound CPD lesion.

The 5WC is reordered at 500 ns (**Fig. 5C**), when the isoalloxazine ring of $FADH^-$ has returned to its relaxed fully reduced state. Accordingly, the **Con2b** intermediate can be understood as the "enzyme-recovered product complex" prior to initiation of product release. In the N100ns snapshot (**Con2a**) the 5WC adopts a slightly different geometry when compared to both the dark and N500ns states, which apparently represents a structural snapshot of the process towards the enzyme-recovered product complex. The concept of enzyme recycling is well known, but it is notable that the enzyme does not rush to release the product before resetting the conformations of its active site moieties that have been altered during catalysis. In this way, the enzyme may drive product release, while being primed for cognate substrate recognition and the next reaction cycle.

Role of the BIR during product release by photolyases

While the 5WC/R256 locus is involved in fine-steering the active site's affinity for cognate CPD substrates and repaired products, the BIR acts in stabilizing the unpaired bubble of the bound dsDNA, i.e. the DNA region vacated by CPD flip-out upon binding to *Mm*CPDII (**Fig. 2E**) (*43*). Unlike the 5WC/R256 locus, the BIR locus remains essentially unchanged during the first 500 ns (**Fig. 5D, fig. S11**), but shows first, only slight changes for the N25μs snapshot (**Con3a**) and, as expected, large-scale changes in both complexes of the N200μs snapshot, where the two thymines have partially entered the unpaired bubble (**Con3b** and **Con4**, **Figs. 5E, 5F**, **fig. S7, fig. S11**). As

the 5'-thymine first flips back towards the unpaired bubble (**Fig. 5E**), the resulting rotation of the intra-CPD phosphate causes BIR residue R441 to swivel away from the phosphate by changing its center of mass distance from 4.4 Å to 7.2 Å (**Fig. 5E**). This opens the BIR "lock" and allows both thymines to return sequentially to the unpaired bubble. Once filling the unpaired bubble, the two thymine bases stack well with the preceding dC6 base and interact with their complementary bases dA7' and dA8', essentially displacing D428 and R429, while R441 moves back closer to the dT8 phosphate, stabilizing it in its new orientation (**Fig. 5F**). However, the remaining BIR element W431 remains interacting with dC9 and the thymine bases, which rationalizes why the repaired DNA, after losing so many interactions at the active site, still sticks to the enzyme before full release, and why the bound and still kinked DNA at this point is highly dynamic as shown by the large number of diffuse difference density peaks around the DNA backbone (**Fig. 4E**, right structure). Indeed, clustering analysis of steered molecular dynamics simulations restrained by the ΔFo(200μs-dark) electron density map revealed that dsDNA in complex A adopts a single major conformation similar to the starting structure (**fig. S12**). In contrast, the dsDNA of complex B showcases two major conformations with different degrees of deformation in the unpaired bubble region, supporting that DNA release starts at the unpaired bubble, and extends from it towards the upstream and downstream regions of the DNA (**fig. S12**).

Upon full DNA release, even this last protein-DNA interaction will be broken, and dC9 and -T-T- co-stack again as in canonical dsDNA. It is feasible that CPD-DNA binding by *Mm*CPDII follows the reverse sequence of events: First, W431 intercalates between the 3'-thymine of the CPD lesion and its downstream base enforcing suboptimal base stacking on both sides of the CPD lesion. Then, an onset of interactions between R429 and the counterbases dA7' and dA8' (*37*) supplies further stabilization. Finally, the R441-D428 lock facilitates CPD phosphate rotation, thus causing the CPD flip into the enzyme's active site.

Overall, our results not only characterized the intermediates of TT-dimer repair, but also demonstrated the associated dynamic processes of key active site moieties. Furthermore, we have identified and characterized intermediates in the entire catalytic process in addition to chemical steps, and rationalized how damaged dsDNA binds to the active site, gets repaired, how the enzyme recovers, and then how the repaired bases return to dsDNA during product release.

Complementary approaches to validate the TR-SFX derived photolyase mechanism

To provide further support, we performed three additional analyses on the structural TR-SFX data as a whole, with details provided in **Supplementary Texts S4-S6**. First, we developed a kinetic model (**Supplementary Text S4** and **fig. S13A**) based on the accumulation of negative densities around the two affected bonds, C5-C5' and C6-C6' during the first 3.35 ns of the reaction (**Fig. 3B**, **fig. S13B**). By numerical integration of this model, we could determine that indeed **Int3**, i.e. $(T\_T)^{\bullet-}$, was the dominant species between 450 to 650 ps, while a mixture of **Int4** and **Int5** became dominant after 1 ns (**fig. S13C**), as described by our molecular structures (**Fig. 3A**). These results show that the kinetic data derived from the negative density accumulation correlate well with the derived intermediate structures and thus produce a valid reaction mechanism (**fig. S13D**).

Second, we performed singular value decomposition (SVD) analysis of both the ps-ns and ns-µs time-series as described in **Supplementary Text S5**, **fig. S14** and **S15**. For the ns-ps series, the first main component (lSV1) acted by symmetrically separating the CPD bases, while the second one (lSV2) dampened the effect of the first one in the vicinity of C6-C6', effectively delaying their separation (**fig. S14A and B**). Meanwhile, SVD results for the ns-µs series agreed very well with our molecular structures (**Fig. 4**), and supported a three-state mechanism for DNA release. Here, the first component effectively represented local CPD changes prevalent at 100 to 500 ns (lSV1), the second global DNA changes during complex release at 200 µs (lSV2), and the final one base flip-back between 25 and 200 µs (lSV3) (**fig. S15**). Since SVD is performed over the entire asymmetric unit including complexes A and B, we performed further structural analyses to show that complexes A and B of 200 µs involve shifts of populations (**fig. S7**).

Third, we sought to validate our interpretations of time-dependent structural changes via QM computational analysis by using the density functional theory (DFT) method to calculate the highest occupied molecular orbitals (HOMO) of the TR-SFX derived atomic coordinates of CPD repair intermediates (**Supplementary Text S6** and **fig. S16A**). Our data showed overlapping orbitals up to 650 ps (**Int3**) and formation of a node at 1 ns (**Int4**, **fig. S16B**), supporting complete rupture of the cyclobutane ring between 650 ps and 1 ns. Furthermore, when the calculation was repeated with addition of a negative charge to CPD, node formation then occurred at 3.35 ns, i.e. BET involving **Int4** and **Int5** (**fig. S16C**), reflecting the extra time needed for back electron transfer.

Discussion

Comparing TR-SFX data with kinetic data from spectroscopic studies of photolyases

Even though this work focussed on structural details of the intermediates and processes during catalysis of DNA repair by a class II photolyase, the kinetics and order of occurrence of intermediate species should resemble that from spectroscopic studies in solution, though detailed data can differ due to different experimental conditions and sample sources. Overall, our results are in close agreement with results of previous ultrafast time-resolved spectroscopic studies, wherever a comparison can be made, such as the chemical structures of the intermediates of cyclobutane repair (*22*, *25*, *57*), and the roles of active site residues such as R256 and hydration dynamics (*56*). The role of primary hydration dynamics in stabilizing and mediating the charge transfer reactions, which had been previously hypothesized based on ultrafast spectroscopic analysis of the DNA repair reaction (*25*), has been now given a molecular and structural basis. Here, the R256-5WC locus plays a key role in stabilizing the negative charge of the electron that travels back and forth between the $FADH^{\bullet}$ coenzyme and the CPD lesion. In addition, while the exact timing of each step may differ between our TR-SFX study and previous spectroscopic studies due to different conditions and/or model systems used, e.g. double-stranded CPD-DNA vs. UV-damaged oligo-dT, the relative timing of different steps is in very good agreement.

Furthermore, we can also address some of the differences in the kinetics and quantum yields reported previously for different photolyases. For example, our data clearly indicate that the occupancy of activated complexes during CPD repair stays constant from 100 ps to 10 ns (**table S1**). This signifies that, once FET has occurred, the reaction proceeds with almost 100% efficiency and, conversely, that the observed quantum yields for repair depend on non-productive de-excitation of $FADH^{\bullet}$*. Another possible culprit for lowered quantum yields is the proposed intramolecular ET (iET) between the $FADH^{\bullet}$ isoalloxazine and adenine moieties (*41*, *60*). We believe that the latter is a plausible explanation, although our data showed no significant time-dependent conformational changes around the adenine moiety. iET is part of the FET pathway in class II photolyase mediated DNA repair, but not predominant in class I photolyases (*41*). This hypothesis, which also implies that iET is completed within the overall FET time-frame of about 100-250 ps, fits well with the comparatively low quantum yield of *Mm*CPDII (~25%, **fig. S18**) compared to yields of 45–100 % reported for class I photolyases (*40*, *61*). These results suggest

that different photolyases, despite high structural homology, differ in their kinetic schemes, as also reflected by the variations of kinetic constants and quantum yields depending on class, species, substrate, and reaction conditions (*41*, *57*, *60*, *62*). Since our TR-SFX analysis of *Mm*CPDII simultaneously examined multiple reaction loci, as well as chemical and conformational properties, the order of events found in this study should reflect the real time events, though it was not our intention to determine detailed kinetic constants. Nevertheless, our finding that BET occurs 1-2 ns after photon absorption and FET (**Fig. 3B**) is comparable to previous reports about class II photolyases, where $(T+T)^{\bullet-}$ appeared ~600 ps after photon absorption, and BET was completed 850 ps later (*21*).

Prior spectroscopic data had suggested that bond breaking occurred sequentially, with C5-C5' breaking first, followed by C6-C6' (**Fig. 1A**) (*22*, *23*, *25*, *28*, *59*). Our results have validated this mechanism and characterized the chemical structure of the ring opening intermediate in the enzyme bound form.

The issue of multiphoton effects on DNA repair by photolyases

While it is conceivable that FAD dynamics, particularly the resulting FET kinetics, is affected by multiphoton excitation, the focus of this work is the repair of CPD-lesion comprising DNA, which should be minimally affected, if at all, by multiphoton effects based on the following mechanistic and experimental considerations.

First, the structural moiety being repaired, CPD, does not interact at 400 nm with the excitation light. Initiation of its repair only requires an electron via FET from the excited $FADH^{-*}$. Since our results show that FET is completed in ~250 ps, whereas CPD repair takes place mainly during 0.45-1.0 ns, the repair mechanism itself should be unaffected by the mechanism and kinetics of FET. Previous spectroscopic studies showed that electronic relaxation of free $FADH^{-*}$ proceeds within 5-10 ps, but takes about 1.8 ns when bound to free photolyases (*27*), indicating sufficient time for generating higher states than S1 by excitation of $FADH^{-*}$. However, relaxation of $FADH^{-*}$ from higher states, i.e. S2 and higher, occurs within a few ps (*45*) or even faster by internal conversion. Even if multiple photon absorbtion by $FADH^-$ may cause high-energy states, which eject a free electron by reaching the ionization continuum, this process might be biologically feasible. In the presence of the 8-hydroxy-deazaflavin antenna chromophore, light energy absorbed by the antenna is predicted to cause free electron ejection from $FADH^-$ by a process called

intermolecular coulombic decay, ICD (*63*). Although the effects on quantum yield cannot be discounted, those on the FET speed appear rather unlikely according to our TR-SFX data, as previously published FET time constants from time-resolved spectroscopy range between 200 to 600 ps, e.g. 209 ps for a class I and 565 ps for a class II photolyase (*41*). Thermal effects caused by vibrational cooling upon back-conversion of high-energy states of $FADH^{-*}$ are also unlikely to affect catalysis as we did not observe any kind of conformational changes for the photolyase-DNA complex in its oxidized state under multiphoton conditions (**fig. S1A, B**).

Second, the interpretation of our results is based on multiple active site moieties (**Fig. 2A-E**) that all display different time-dependent changes. As mentioned above, CPD repair is by orders of magnitude slower than multiphoton relaxation. Based on **Fig. 6A**, the recovery of active site residue conformations (500 ns) and the thymine back-flipping and product return (microsecond range) are even slower, thus unlikely to be affected by any multiphoton effect.

Third, it is interesting to note the high degree of correlation between the CPD ΔFo features in the F10ns and N10ns snapshots (**Materials and methods summary**). Since simultaneous multiphoton excitation may occur in the ps-ns series (pulse duration: 0.98 ps), but not in the ns-µs series due to long pulse duration (3 ns) as addressed in **Supplementary Text S3**, we would expect that the F10ns and N10ns snapshots and their difference maps differ significantly, if multiphoton excitation affected repair kinetics in the ps-ns series.

Finally, as described in the beginning of Results, power titration results suggested that the power used in our experiments are just enough, in contrast to the calculated values suggesting excessive photons. This disparity has also been reported recently (*64*), suggesting that far fewer photons than the nominal values are absorbed for reasons requiring further investigation. An alternative scenario, especially for proteins optimized for light-driven electron transfer, is that "proteins may have evolved to direct all deposited energy toward functional outcomes" (*46*, *50*).

The issue of identifyable reaction intermediates from TR-SFX experiments

While many TR-SFX reports focused on dynamic features of a specific chemical or physical step (*6*, *10*, *49*, *65*), and some others used kinetic models from spectroscopic studies to guide their search for reaction intermediates (*20*), our work dealt with an entire catalytic cycle with many elementary steps not assigned before, like ordered product release. In the following, we address some of the general issues encountered in our work. Intermediates of chemical or enzymatic

reactions are commonly considered stable enough when being detectable by kinetic or biophysical methods. These methods are usually limited by their capacity to detect characteristic signals for each intermediate moiety, and thus provide mostly local information about the reactants themselves. Notably, the IUPAC Gold Book (*66*) defines an intermediate as "a molecular entity with a lifetime appreciably longer than a molecular vibration that is formed from the reactants and reacts further to give the products of a chemical reaction". Since TR-SFX captures global information about all atoms within the enzyme-substrate complex, in our case a photolyase bound to the biopolymeric CPD-DNA, it should be able to unravel multiple intermediates, or molecular entities, in a chemical step or a process (e.g. conformational change, product release) particularly since they can be stabilized by the enzyme. This is what we have accomplished in this work, as summarized in **Table 1**.

On the other hand, since each time point may consist of multiple intermediates with varying populations, each snapshot listed in **Table 1** represents either the predominant species of that particular snapshot or a mixture of species. Importantly, we based our assignments not only on the refined structural models, but also on the features of the ΔFo maps, such as C-C peak distances and accumulation of negative densities along the relevant bonds (**Fig. 3B**). These assignments were then further validated by other relevant structural changes at the active site, such as the status of the dihedral angles of the FAD and the structural movements of the 5WC/R256 locus (**Table 1**), and by different experimental approaches (**Supplementary Texts S4-S6**).

Furthermore, the reliability and significance of the refined structural changes is supported by correlation coefficient analysis (**fig. S6**), which quantifies the similarity between the observed and calculated difference electron density maps. Here, and especially within the initial 2 ns, where prior solution spectroscopic studies predicted that most chemical changes would occur (*40, 58*), individual structures strongly correlated with their corresponding density maps, but not with those of their neighbouring time-points, suggesting that each snapshot harboured mostly a distinct conformation.

A conformational change is commonly considered as a simple two-state process, where a time-dependent structural change corresponds to a shift of population between two states. In our view, a conformational change could be a continuous or multi-step process, as demonstrated recently by a temperature-resolved cryo-EM study of a ligand-induced conformational change of another enzyme (*67*). In the present work, we found that the active site of the enzyme goes through

a multi-step process (10 ns – 500 ns) to recover from catalysis, and we identified two variants, **Con2a** and **Con2b** in the process. For the product release, we also identified two variants (**Con3a** and **Con3b**) in the process of back-flipping of the repaired thymines, and characterized the reannealed product **Con4**. Interestingly, increased conformational freedom around the DNA leads to the shift of population between **Con3b** and **Con4** (**fig. S7**).

In summary, for the CPD repair in the ps-ns series, the structure from a snapshot often consists of multiple intermediates. Those with distinct structures in a predominant state can be well characterized, such as the ring opening intermediates in the F650ps (C5-C5' cleaved) and F1ns (C6-C6' also cleaved) snapshots. Those of the electron transfer processes (FET, BET) are not directly resolvable by TR-SFX before occurrence of the next step. However, the ET processes can be indirectly identified from changes in the coenzyme and active site residues.

A new era in enzymology: watching multi-step catalysis as a whole in real time

Our results described in this work are summarized in an overall time line (**Fig. 6A**) by a molecular movie (**Fig. 6B**, or **Video S1**). Real-time recording of molecular movies such as this signals a new era in describing the processes and structural basis of (photo)enzymatic catalysis, particularly for the multi-step reactions catalyzed by photolyases. Here, FET reaction leads to accumulation of bond-cleavage intermediates, followed by ring opening, BET, post-repair recovery of enzyme and coenzyme, and thymine back-flip and DNA release. The events of CPD repair are mediated by structural fluctuations of the FAD coenzyme and the surrounding active site moieties including the 5WC/R256 locus, whereas thymine back-flip and the onset of DNA release proceed along the BIR region of the unpaired bubble. Interestingly, we also observed the directionality of DNA repair, i.e. the 5'-T moves away from the 3'-T after opening of the CPD ring so that the 5'-T leaves the active site first.

Materials and methods summary

Sample preparation

*Mm*CPDII-DNA co-crystals were grown according to previously published conditions (*37*, *43*) after applying further optimizations for enzyme activity and large-scale microcrystal production.

Here, the *Mm*CPDII protein solution was directly activated prior to crystallization via photoreduction in the presence of DTT, white light and under anaerobic conditions, followed by mixing with CPD-containing DNA. After an incubation period of ~2 h at 23 °C, crystals were harvested, mixed with grease and loaded into injectors according to previously established protocols (*68*). To preserve enzyme activity, all steps were performed under anaerobic conditions in a COY Labs vinyl anaerobic chamber. Further, to prevent accidental DNA repair, all experimental steps after enzyme photoreduction were performed under safety light (640 nm). To confirm enzyme status, in-solution reoxidation was followed by UV-Vis absorption spectroscopy (**fig. S17A**), which showed that *Mm*CPDII remained in the fully reduced state under experimental conditions for at least 24 hours after photoreduction. Although the presence of photodamaged DNA is known to further stabilize $FADH^-$ in photolyases, we further confirmed *Mm*CPDII *in crystallo* status via *in crystallo* UV-Vis absorption spectroscopy of 20-hour old crystals (**fig. S17B**). No crystals older than 20 hours were used for any of the experiments presented in this work. Further details for sample preparation can be consulted in Supplementary methods.

Data collection

At SACLA (*69*), data was collected at the BL2 beamline using a 30 Hz pulse frequency and 10 keV X-ray with a pulse duration of <10 fs and focused to a focal spot with a diameter of 1.5 µm. For time-resolved experiments, a 15 Hz, 150 µJ, 408 nm OPO pump laser with a 3 ns pulse length with a 100 µm diameter focal spot was used. During all experiments, the DAPHNIS (*70*) chamber was flooded with a 98% helium atmosphere to increase signal to noise ratio, and to prevent oxidation of the sample. Samples were extruded at 2.6 µL/min through a 75 µm nozzle (*71*). Images were collected on a short-working distance octal multi-port detector with 50 mm sample to detector distance (*72*). Initial light and dark splitting as well as initial processing was performed by the Cheetah pipeline (*73*).

At SwissFEL (*74*), the XFEL was also 1.5 µm in diameter with a ~20 fs pulse duration, but run at 100 Hz. For time-resolved data collection, the in-house laser was set for a pulse duration of 0.98 ps, with a pulse energy of 10 µJ and a focal spot diameter of 50 µm running in a 3:1 setup. Accordingly, for every three light images, one dark image was collected. Sample was extruded at 5 µL/min through a 75 µm nozzle, while the chamber was maintained at 200 mbar after flooding and evacuating three times with helium.

The average crystal size was 50x50x50 μm^3 with an 1/e penetration depth of 103 µm at 400 nm. Further details and control experiments for light contamination and laser power can be found in **Supplementary methods**, **Supplementary Texts 1-3** and **figs. S1-S3**.

Processing, refinement and analysis

Data processing with CrystFEL (*75*, *76*) and refinement procedures are described in detail in Supplementary methods. Briefly, we followed previously described guidelines (*5*, *9*, *52*, *53*) to perform structure factor extrapolation followed by structural refinement (**tables S1-S2** for refinement statistics). Additionally, two features were given particular attention, namely the exact structure of the CPD cyclobutane ring (**Fig. 1A**) and the dihedral angles ρ_C and ρ_N of the FAD isoalloxazine moiety (**Fig. 1C**). To accurately determine the crucial CPD and FAD geometries, we performed real-space correlation-coefficient (CC) based refinement of both features. Here, we searched for maximum correlation between a ΔFo(Y-X) map and an equivalent calculated difference map (ΔFc(Y-X)) based on a fully refined static structure (X) and the time-resolved structure to be refined (Y). This approach produces a quantitative quality parameter, CC, which can be compared for a given structure versus all experimental data to quantify how well small structural changes, such as bond elongation during CPD repair, can be monitored in our time courses (**fig. S6**). Our occupancies achieved by light-triggering (**tables S1-S2**) are close to the experimental quantum yield of 24±1% for DNA repair by *Mm*CPDII (**fig. S18**, **table S3**) for the ns-µs series (20-22%) and about half of that for ps-ns series (11-13%).

The asymmetric unit contains two complexes. Unless otherwise stated, the maps shown in the figures are always from complex A, since those of complex B are much noisier than complex A (I/σ values of 3 or below).

Consistency between F series and N series

In order to control for consistency between the ps-ns and ns-µs series, we collected the 10 ns time-point both at SwissFEL and SACLA. Two important factors need to be considered when comparing these two 10 ns snapshots. The first one is resolution. Given the lower resolution of N10ns (2.7 Å), atomic positions are less well defined than in the high-resolution counterpart F10ns (2.15 Å). Secondly, and more importantly, is pulse duration. For the F10ns snapshot, each crystal is illuminated for 0.98 ps, while for N10ns, for 3 ns. Accordingly, reaction coherence is higher in

F10ns than in N10ns. For example, the variance for the ps-ns series is expected to be ±0.001 ns, i.e. the pump pulse duration. Meanwhile, in the ns-µs series, the variance could amount up to ±3 ns, i.e. an error of 30% relative to N10ns, which decreases for longer delay times. Accordingly, the N10ns snapshot corresponds more to a mixture of the F6ns and F10ns snapshots, implying that their correlation coefficients around the CPD are all the same (N10ns/F6ns: 0.62; N10ns/F10ns: 0.61, F6ns/F10ns: 0.67).

Calculation of C-C peak distances

Bias-free monitoring of distances between peaks from difference maps is more reliable than atom-atom distances from refined structural models in tracking structural changes by TR-SFX. In our study, only the 5'-T, not the 3'-T appears to move upon opening of the cyclobutane, leading to mainy negative peaks for the cyclobutane and positive peaks at the 5'-T side. To determine the distance between the negative cyclobutane and the positive 5'-T difference density peaks along the C5-C5' and C6-C6' bonds, ΔFo maps were generated with the phenix isomorphous difference tool as described in **Supplementary Materials** and shown in **Figures 3A and 4**. The CCP4 tool fft was then used to extract electron densities at a 2.5 σ contour level. To ensure an identical number of voxels existed in each map even at different resolutions, the grid was set to 1/4 x maximum resolution. Next, a Python script was used first to position a dummy atom on the C5 and C6 positions, and then to move them along the C5-C5' and the C6-C6' bond axises in steps of 0.385 Å (half the atomic radius of carbon) for 11 steps (4.235 Å) towards, and beyond, the 5'-T. In both cases, the dummy atom was then used as a mask to extract the integrated electron density at each position and plotted versus distance (**fig. S5**). The distance between minimum (cyclobutane peak) vs. maximum (5'-T peak) along each axis was then extracted from the plots. Importantly, if either a minimum or a maximum could not be determined, no peak distance could be calculated, and therefore no value was assigned (noted as a dash "-" on **Table 1**), or plotted (**Figs. 3B and 4B**).

REFERENCES AND NOTES

1. A. Merk, A. Bartesaghi, S. Banerjee, V. Falconieri, P. Rao, M. I. Davis, R. Pragani, M. B. Boxer, L. A. Earl, J. L. S. Milne, S. Subramaniam, Breaking Cryo-EM Resolution Barriers to Facilitate Drug Discovery. *Cell*. **165**, 1698–1707 (2016).
2. M. D. Tsai, W. J. Wu, M. C. Ho, Enzymology and Dynamics by Cryogenic Electron Microscopy. *Annu. Rev. Biophys.* **51**, 19–38 (2022).
3. H. N. Chapman, X-ray free-electron lasers for the structure and dynamics of macromolecules. *Annu. Rev. Biochem.* **88**, 35–58 (2019).
4. M. A. Wilson, Mapping Enzyme Landscapes by Time-Resolved Crystallography with Synchrotron and X-Ray Free Electron Laser Light. *Annu. Rev. Biophys.* **51**, 79–98 (2022).
5. M. Schmidt, Time-resolved macromolecular crystallography at pulsed X-ray sources. *Int. J. Mol. Sci.* **20**, 1401 (2019).
6. P. Nogly, T. Weinert, D. James, S. Carbajo, D. Ozerov, A. Furrer, V. Borin, P. Skopintsev, K. Jaeger, K. Nass, P. Båth, R. Bosman, M. Seaberg, T. Lane, D. Kekilli, S. Brünle, T. Tanaka, W. Wu, C. Milne, T. White, A. Barty, U. Weierstall, V. Panneels, E. Nango, M. Jacobs, M. Lopez-garcia, O.-P. Prathep, T. Lawson, R. Oulton, H. M. Whitney, Retinal isomerization in bacteriorhodopsin captured by a femtosecond x-ray laser. *Science*. **361**, eaat0094 (2018).
7. E. Nango, A. Royant, M. Kubo, T. Nakane, C. Wickstrand, T. Kimura, T. Tanaka, K. Tono, C. Song, R. Tanaka, T. Arima, A. Yamashita, J. Kobayashi, T. Hosaka, E. Mizohata, P. Nogly, M. Sugahara, D. Nam, T. Nomura, T. Shimamura, D. Im, T. Fujiwara, Y. Yamanaka, B. Jeon, T. Nishizawa, K. Oda, M. Fukuda, R. Andersson, P. Båth, R. Dods, J. Davidsson, S. Matsuoka, S. Kawatake, M. Murata, O. Nureki, S. Owada, T. Kameshima, T. Hatsui, Y. Joti, G. Schertler, M. Yabashi, A.-N. Bondar, J. Standfuss, R. Neutze, S. Iwata, A three-dimensional movie of structural changes in bacteriorhodopsin. *Science*. **354**, 1552–1557 (2016).
8. J. Tenboer, S. Basu, N. Zatsepin, K. Pande, D. Milathianaki, M. Frank, M. Hunter, S. Boutet, G. J. Williams, J. E. Koglin, D. Oberthuer, M. Heymann, C. Kupitz, C. Conrad, J. Coe, S. Roy-Chowdhury, U. Weierstall, D. James, D. Wang, T. Grant, A. Barty, O. Yefanov, J. Scales, C. Gati, C. Seuring, V. Srajer, R. Henning, P. Schwander, R. Fromme, A. Ourmazd, K. Moffat, J. J. Van Thor, J. C. H. Spence, P. Fromme, H. N. Chapman, M. Schmidt, Time-resolved serial crystallography captures high-resolution intermediates of photoactive yellow protein. *Science*. **346**, 1242–1246 (2014).
9. E. Claesson, W. Y. Wahlgren, H. Takala, S. Pandey, L. Castillon, V. Kuznetsova, L. Henry, M. Panman, M. Carrillo, J. Kübel, R. Nanekar, L. Isaksson, A. Nimmrich, A. Cellini, D. Morozov, M. Maj, M. Kurttila, R. Bosman, E. Nango, R. Tanaka, T. Tanaka, L. Fangjia, S. Iwata, S. Owada, K. Moffat, G. Groenhof, E. A. Stojković, J. A. Ihalainen, M. Schmidt, S. Westenhoff, The primary structural photoresponse of phytochrome proteins captured by a femtosecond x-ray laser. *Elife*. **9**, 1–18 (2020).
10. N. Coquelle, M. Sliwa, J. Woodhouse, G. Schirò, V. Adam, A. Aquila, T. R. M. Barends, S. Boutet, M. Byrdin, S. Carbajo, E. D. La Mora, R. B. Doak, M. Feliks, F. Fieschi, L. Foucar, V. Guillon, M. Hilpert, M. S. Hunter, S. Jakobs, J. E. Koglin, G. Kovacsova, T. J. Lane, B. Lévy, M. Liang, K. Nass, J. Ridard, J. S. Robinson, C. M. Roome, C. Ruckebusch, M. Seaberg, M. Thepaut, M. Cammarata, I. Demachy, M. Field, R. L. Shoeman, D. Bourgeois, J. P. Colletier, I. Schlichting, M. Weik, Chromophore twisting in the excited state of a photoswitchable fluorescent protein captured by time-resolved serial femtosecond crystallography. *Nat. Chem.* **10**, 31–37 (2018).
11. S. Mous, G. Gotthard, D. Ehrenberg, S. Sen, T. Weinert, P. J. M. Johnson, D. James, K. Nass, A. Furrer, D. Kekilli, P. Ma, S. Brünle, C. Maria Casadei, I. Martiel, F. Dworkowski, D. Gashi, P. Skopintsev, M. Wranik, G. Knopp, E. Panepucci, V. Panneels, C. Cirelli, D. Ozerov, G. F. X. Schertler, M. Wang, C. Milne, J. Standfuss, I. Schapiro, J. Heberle, P. Nogly, Dynamics and mechanism of a light-driven chloride pump. *Science*. **375**, 845–851 (2022).
12. P. Skopintsev, D. Ehrenberg, T. Weinert, D. James, R. K. Kar, P. J. M. Johnson, D. Ozerov, A. Furrer, I. Martiel, F. Dworkowski, K. Nass, G. Knopp, C. Cirelli, C. Arrell, D. Gashi, S. Mous, M. Wranik, T. Gruhl, D. Kekilli, S. Brünle, X. Deupi, G. F. X. Schertler, R. M. Benoit, V. Panneels, P. Nogly, I.

Schapiro, C. Milne, J. Heberle, J. Standfuss, Femtosecond-to-millisecond structural changes in a light-driven sodium pump. *Nature*. **583**, 314–318 (2020).
13. A. Bhowmick, R. Hussein, I. Bogacz, P. S. Simon, M. Ibrahim, R. Chatterjee, M. D. Doyle, M. H. Cheah, T. Fransson, P. Chernev, I. S. Kim, H. Makita, M. Dasgupta, C. J. Kaminsky, M. Zhang, J. Gätcke, S. Haupt, I. I. Nangca, S. M. Keable, A. O. Aydin, K. Tono, S. Owada, L. B. Gee, F. D. Fuller, A. Batyuk, R. Alonso-Mori, J. M. Holton, D. W. Paley, N. W. Moriarty, F. Mamedov, P. D. Adams, A. S. Brewster, H. Dobbek, N. K. Sauter, U. Bergmann, A. Zouni, J. Messinger, J. Kern, J. Yano, V. K. Yachandra, Structural evidence for intermediates during O2 formation in photosystem II. *Nature*. **617**, 629–636 (2023).
14. J. Kern, R. Chatterjee, I. D. Young, F. D. Fuller, L. Lassalle, M. Ibrahim, S. Gul, T. Fransson, A. S. Brewster, R. Alonso-Mori, R. Hussein, M. Zhang, L. Douthit, C. de Lichtenberg, M. H. Cheah, D. Shevela, J. Wersig, I. Seuffert, D. Sokaras, E. Pastor, C. Weninger, T. Kroll, R. G. Sierra, P. Aller, A. Butryn, A. M. Orville, M. Liang, A. Batyuk, J. E. Koglin, S. Carbajo, S. Boutet, N. W. Moriarty, J. M. Holton, H. Dobbek, P. D. Adams, U. Bergmann, N. K. Sauter, A. Zouni, J. Messinger, J. Yano, V. K. Yachandra, Structures of the intermediates of Kok's photosynthetic water oxidation clock. *Nature*. **563**, 421 (2018).
15. I. D. Young, M. Ibrahim, R. Chatterjee, S. Gul, F. D. Fuller, S. Koroidov, A. S. Brewster, R. Tran, R. Alonso-Mori, T. Kroll, T. Michels-Clark, H. Laksmono, R. G. Sierra, C. A. Stan, R. Hussein, M. Zhang, L. Douthit, M. Kubin, C. De Lichtenberg, L. Vo Pham, H. Nilsson, M. H. Cheah, D. Shevela, C. Saracini, M. A. Bean, I. Seuffert, D. Sokaras, T. C. Weng, E. Pastor, C. Weninger, T. Fransson, L. Lassalle, P. Bräuer, P. Aller, P. T. Docker, B. Andi, A. M. Orville, J. M. Glownia, S. Nelson, M. Sikorski, D. Zhu, M. S. Hunter, T. J. Lane, A. Aquila, J. E. Koglin, J. Robinson, M. Liang, S. Boutet, A. Y. Lyubimov, M. Uervirojnangkoorn, N. W. Moriarty, D. Liebschner, P. V. Afonine, D. G. Waterman, G. Evans, P. Wernet, H. Dobbek, W. I. Weis, A. T. Brunger, P. H. Zwart, P. D. Adams, A. Zouni, J. Messinger, U. Bergmann, N. K. Sauter, J. Kern, V. K. Yachandra, J. Yano, Structure of photosystem II and substrate binding at room temperature. *Nature*. **540**, 453–457 (2016).
16. C. Kupitz, S. Basu, I. Grotjohann, R. Fromme, N. A. Zatsepin, K. N. Rendek, M. S. Hunter, R. L. Shoeman, T. A. White, D. Wang, D. James, J. H. Yang, D. E. Cobb, B. Reeder, R. G. Sierra, H. Liu, A. Barty, A. L. Aquila, D. Deponte, R. A. Kirian, S. Bari, J. J. Bergkamp, K. R. Beyerlein, M. J. Bogan, C. Caleman, T. C. Chao, C. E. Conrad, K. M. Davis, H. Fleckenstein, L. Galli, S. P. Hau-Riege, S. Kassemeyer, H. Laksmono, M. Liang, L. Lomb, S. Marchesini, A. V Martin, M. Messerschmidt, D. Milathianaki, K. Nass, A. Ros, S. Roy-Chowdhury, K. Schmidt, M. Seibert, J. Steinbrener, F. Stellato, L. Yan, C. Yoon, T. A. Moore, A. L. Moore, Y. Pushkar, G. J. Williams, S. Boutet, R. B. Doak, U. Weierstall, M. Frank, H. N. Chapman, J. C. H. Spence, P. Fromme, Serial time-resolved crystallography of photosystem II using a femtosecond X-ray laser. *Nature*. **513**, 261–265 (2014).
17. M. Suga, F. Akita, K. Yamashita, Y. Nakajima, G. Ueno, H. Li, T. Yamane, K. Hirata, Y. Umena, S. Yonekura, L. J. Yu, H. Murakami, T. Nomura, T. Kimura, M. Kubo, S. Baba, T. Kumasaka, K. Tono, M. Yabashi, H. Isobe, K. Yamaguchi, M. Yamamoto, H. Ago, J. R. Shen, An oxyl/oxo mechanism for oxygen-oxygen coupling in PSII revealed by an x-ray free-electron laser. *Science*. **366**, 334–338 (2019).
18. A. Shimada, M. Kubo, S. Baba, K. Yamashita, K. Hirata, G. Ueno, T. Nomura, T. Kimura, K. Shinzawa-Itoh, J. Baba, K. Hatano, Y. Eto, A. Miyamoto, H. Murakami, T. Kumasaka, S. Owada, K. Tono, M. Yabashi, Y. Yamaguchi, S. Yanagisawa, M. Sakaguchi, T. Ogura, R. Komiya, J. Yan, E. Yamashita, M. Yamamoto, H. Ago, S. Yoshikawa, T. Tsukihara, A nanosecond time-resolved XFEL analysis of structural changes associated with CO release from cytochrome C oxidase. *Sci. Adv.* **3**, e1603042 (2017).
19. I. Ishigami, A. Lewis-Ballester, A. Echelmeier, G. Brehm, N. A. Zatsepin, T. D. Grant, J. D. Coe, S. Lisova, G. Nelson, S. Zhang, Z. F. Dobson, S. Boutet, R. G. Sierra, A. Batyuk, P. Fromme, R. Fromme, J. C. H. Spence, A. Ros, S. R. Yeh, D. L. Rousseau, Snapshot of an oxygen intermediate in the catalytic reaction of cytochrome c oxidase. *Proc. Natl. Acad. Sci. U. S. A.* **116**, 3572–3577 (2019).
20. D. Sorigué, K. Hadjidemetriou, S. Blangy, G. Gotthard, A. Bonvalet, N. Coquelle, P. Samire, A. Aleksandrov, L. Antonucci, A. Benachir, S. Boutet, M. Byrdin, M. Cammarata, S. Carbajo, S. Cuiné,

R. B. Doak, L. Foucar, A. Gorel, M. Grünbein, E. Hartmann, R. Hienerwadel, M. Hilpert, M. Kloos, T. J. Lane, B. Légeret, P. Legrand, Y. Li-Beisson, S. L. Y. Moulin, D. Nurizzo, G. Peltier, G. Schirò, R. L. Shoeman, M. Sliwa, X. Solinas, B. Zhuang, T. R. M. Barends, J.-P. Colletier, M. Joffre, A. Royant, C. Berthomieu, M. Weik, T. Domratcheva, K. Brettel, M. H. Vos, I. Schlichting, P. Arnoux, P. Müller, F. Beisson, Mechanism and dynamics of fatty acid photodecarboxylase. *Science*. **372**, eabd5687 (2021).

21. C. Kupitz, J. L. Olmos, M. Holl, L. Tremblay, K. Pande, S. Pandey, D. Oberthür, M. Hunter, M. Liang, A. Aquila, J. Tenboer, G. Calvey, A. Katz, Y. Chen, M. O. Wiedorn, J. Knoska, A. Meents, V. Majriani, T. Norwood, I. Poudyal, T. Grant, M. D. Miller, W. Xu, A. Tolstikova, A. Morgan, M. Metz, J. M. Martín-García, J. D. Zook, S. Roy-Chowdhury, J. Coe, N. Nagaratnam, D. Meza, R. Fromme, S. Basu, M. Frank, T. White, A. Barty, S. Bajt, O. Yefanov, H. N. Chapman, N. Zatsepin, G. Nelson, U. Weierstall, J. Spence, P. Schwander, L. Pollack, P. Fromme, A. Ourmazd, G. N. Phillips, M. Schmidt, Structural enzymology using X-ray free electron lasers. *Struct. Dyn.* **4**, 44003 (2017).
22. M. Zhang, L. Wang, D. Zhong, Photolyase: Dynamics and electron-transfer mechanisms of DNA repair. *Arch. Biochem. Biophys.* **632**, 158–174 (2017).
23. L. O. Essen, T. Klar, Light-driven DNA repair by photolyases. *Cell. Mol. Life Sci.* **63**, 1266–1277 (2006).
24. P. J. Rochette, S. Lacoste, J. P. Therrien, N. Bastien, D. E. Brash, R. Drouin, Influence of cytosine methylation on ultraviolet-induced cyclobutane pyrimidine dimer formation in genomic DNA. *Mutat. Res. Mol. Mech. Mutagen.* **665**, 7–13 (2009).
25. Y.-T. Kao, C. Saxena, L. Wang, A. Sancar, D. Zhong, Direct observation of thymine dimer repair in DNA by photolyase. *Proc. Natl. Acad. Sci. U. S. A.* **102**, 16128–16132 (2005).
26. K. Brettel, M. Byrdin, Reaction mechanisms of DNA photolyase. *Curr. Opin. Struct. Biol.* **20**, 693–701 (2010).
27. Y. T. Kao, C. Saxena, T. F. He, L. Guo, L. Wang, A. Sancar, D. Zhong, Ultrafast dynamics of flavins in five redox states. *J. Am. Chem. Soc.* **130**, 13132–13139 (2008).
28. A. Sancar, Mechanisms of DNA Repair by Photolyase and Excision Nuclease (Nobel Lecture). *Angew. Chemie - Int. Ed.* **55**, 8502–8527 (2016).
29. A. Sancar, Structure and function of DNA photolyases. *Biochemistry*. **33**, 2–9 (1994).
30. I. Chaves, R. Pokorny, M. Byrdin, N. Hoang, T. Ritz, K. Brettel, L. O. Essen, G. T. J. Van Der Horst, A. Batschauer, M. Ahmad, The cryptochromes: Blue light photoreceptors in plants and animals. *Annu. Rev. Plant Biol.* **62**, 335–364 (2011).
31. C. Aubert, M. H. Vos, P. Mathis, a P. Eker, K. Brettel, Intraprotein radical transfer during photoactivation of DNA photolyase. *Nature*. **405**, 586–590 (2000).
32. A. Sancar, D. Zhong, It is chemistry but not your grandfather's chemistry. *Biochemistry*. **56**, 1–2 (2017).
33. M. Maestre-Reyna, C. H. Yang, E. Nango, W. C. Huang, E. P. G. Ngurah Putu, W. J. Wu, P. H. Wang, S. Franz-Badur, M. Saft, H. J. Emmerich, H. Y. Wu, C. C. Lee, K. F. Huang, Y. K. Chang, J. H. Liao, J. H. Weng, W. Gad, C. W. Chang, A. H. Pang, M. Sugahara, S. Owada, Y. Hosokawa, Y. Joti, A. Yamashita, R. Tanaka, T. Tanaka, F. Luo, K. Tono, K. C. Hsu, S. Kiontke, I. Schapiro, R. Spadaccini, A. Royant, J. Yamamoto, S. Iwata, L. O. Essen, Y. Bessho, M. D. Tsai, Serial crystallography captures dynamic control of sequential electron and proton transfer events in a flavoenzyme. *Nat. Chem.* **14**, 677–685 (2022).
34. A. Cellini, W. Y. Wahlgren, L. Henry, S. Pandey, S. Ghosh, L. Castillon, E. Claesson, H. Takala, J. Kübel, A. Nimmrich, V. Kuznetsova, E. Nango, S. Iwata, S. Owad, E. A. Stojkovic, M. Schmidt, J. A. Ihalainen, S. Westenhoff, The three-dimensional structure of Drosophila melanogaster (6-4) photolyase at room temperature. *Acta Crystallogr. Sect. D Struct. Biol.* **77**, 1001–1009 (2021).
35. A. Cellini, M. K. Shankar, W. Y. Wahlgren, A. Nimmrich, A. Furrer, D. James, M. Wranik, S. Aumonier, E. V Beale, F. Dworkowski, J. Standfuss, T. Weinert, S. Westenhoff, Structural basis of the radical pair state in photolyases and cryptochromes. *Chem. Commun.* **58**, 4889–4892 (2022).
36. R. Kort, H. Komori, S. I. Adachi, K. Miki, A. Eker, DNA apophotolyase from Anacystis nidulans: 1.8 Å structure, 8-HDF reconstitution and X-ray-induced FAD reduction. *Acta Crystallogr. Sect. D Biol. Crystallogr.* **60**, 1205–1213 (2004).

37. S. Kiontke, Y. Geisselbrecht, R. Pokorny, T. Carell, A. Batschauer, L.-O. Essen, Crystal structures of an archaeal class II DNA photolyase and its complex with UV-damaged duplex DNA. *EMBO J.* **30**, 4437–49 (2011).
38. R. Pokorny, T. Klar, U. Hennecke, T. Carell, A. Batschauer, L.-O. L.-O. Essen, Recognition and repair of UV lesions in loop structures of duplex DNA by DASH-type cryptochrome. *Proc. Natl. Acad. Sci. U. S. A.* **105**, 21023–21027 (2008).
39. A. Mees, T. Klar, P. Gnau, U. Hennecke, A. P. M. Eker, T. Carell, L. O. Essen, Crystal structure of a photolyase bound to a CPD-like DNA lesion after in situ repair. *Science*. **306**, 1789–1793 (2004).
40. Z. Liu, C. Tan, X. Guo, Y.-T. Kao, J. Li, L. Wang, A. Sancar, D. Zhong, Dynamics and mechanism of cyclobutane pyrimidine dimer repair by DNA photolyase. *Proc. Natl. Acad. Sci. U. S. A.* **108**, 14831–14836 (2011).
41. M. Zhang, L. Wang, S. Shu, A. Sancar, D. Zhong, Bifurcating electron-transfer pathways in DNA photolyases determine the repair quantum yield. *Science*. **354**, 209–213 (2016).
42. H. J. Park, K. Zhang, Y. Ren, S. Nadji, N. Sinha, J.-S. S. Taylor, C. H. Kang, Crystal structure of a DNA decamer containing a cis-syn thymine dimer. *Proc. Natl. Acad. Sci. U. S. A.* **99**, 15965–15970 (2002).
43. M. Maestre-Reyna, J. Yamamoto, W.-C. Huang, M.-D. Tsai, L.-O. Essen, Y. Bessho, Twist and turn: a revised structural view on the unpaired bubble of class II CPD photolyase in complex with damaged DNA. *IUCrJ*. **5**, 608–618 (2018).
44. S. Weber, Light-driven enzymatic catalysis of DNA repair: a review of recent biophysical studies on photolyase. *Biochim. Biophys. Acta - Bioenerg.* **1707**, 1–23 (2005).
45. R. F. Pauszek, G. Kodali, M. S. U. Siddiqui, R. J. Stanley, Overlapping Electronic States with Nearly Parallel Transition Dipole Moments in Reduced Anionic Flavin Can Distort Photobiological Dynamics. *J. Am. Chem. Soc.* **138**, 14880–14889 (2016).
46. G. Brändén, R. Neutze, Advances and challenges in time-resolved macromolecular crystallography. *Science*. **373**, eaba0954 (2021).
47. E. C. Schulz, B. A. Yorke, A. R. Pearson, P. Mehrabi, Best practices for time-resolved serial synchrotron crystallography. *Acta Crystallogr. Sect. D Struct. Biol.* **78**, 14–29 (2022).
48. A. Gorel, I. Schlichting, T. R. M. Barends, Discerning best practices in XFEL-based biological crystallography – standards for nonstandard experiments. *IUCrJ*. **8**, 532–543 (2021).
49. G. Nass Kovacs, J. P. Colletier, M. L. Grünbein, Y. Yang, T. Stensitzki, A. Batyuk, S. Carbajo, R. B. Doak, D. Ehrenberg, L. Foucar, R. Gasper, A. Gorel, M. Hilpert, M. Kloos, J. E. Koglin, J. Reinstein, C. M. Roome, R. Schlesinger, M. Seaberg, R. L. Shoeman, M. Stricker, S. Boutet, S. Haacke, J. Heberle, K. Heyne, T. Domratcheva, T. R. M. Barends, I. Schlichting, Three-dimensional view of ultrafast dynamics in photoexcited bacteriorhodopsin. *Nat. Commun.* **10**, 1–17 (2019).
50. R. J. D. Miller, O. Paré-Labrosse, A. Sarracini, J. E. Besaw, Three-dimensional view of ultrafast dynamics in photoexcited bacteriorhodopsin in the multiphoton regime and biological relevance. *Nat. Commun.* **11**, 1–4 (2020).
51. M. L. Grünbein, M. Stricker, G. Nass Kovacs, M. Kloos, R. B. Doak, R. L. Shoeman, J. Reinstein, S. Lecler, S. Haacke, I. Schlichting, Illumination guidelines for ultrafast pump–probe experiments by serial femtosecond crystallography. *Nat. Methods*. **17**, 681–684 (2020).
52. M. Carrillo, S. Pandey, J. Sanchez, M. Noda, I. Poudyal, L. Aldama, T. N. Malla, E. Claesson, W. Y. Wahlgren, D. Feliz, V. Šrajer, M. Maj, L. Castillon, S. Iwata, E. Nango, R. Tanaka, T. Tanaka, L. Fangjia, K. Tono, S. Owada, S. Westenhoff, E. A. Stojković, M. Schmidt, High-resolution crystal structures of transient intermediates in the phytochrome photocycle. *Structure*. **29**, 743–754 (2021).
53. J. H. Yun, X. Li, J. Yue, J. H. Park, Z. Jin, C. Li, H. Hu, Y. Shi, S. Pandey, S. Carbajo, S. Boutet, M. S. Hunter, M. Liang, R. G. Sierra, T. J. Lane, L. Zhou, U. Weierstall, N. A. Zatsepin, M. Ohki, J. R. H. Tame, S. Y. Park, J. C. H. Spence, W. Zhang, M. Schmidt, W. Lee, H. Liu, Early-stage dynamics of chloride ion–pumping rhodopsin revealed by a femtosecond X-ray laser. *Proc. Natl. Acad. Sci. U. S. A.* **118**, e2020486118 (2021).
54. M. A. Rould, C. W. Carter, Isomorphous Difference Methods. *Methods Enzymol.* **374**, 145–163 (2003).

55. Y.-T. Kao, C. Tan, S.-H. Song, N. Öztürk, J. Li, L. Wang, A. Sancar, D. Zhong, Ultrafast Dynamics and Anionic Active States of the Flavin Cofactor in Cryptochrome and Photolyase. *J. Am. Chem. Soc.* **130**, 7695–7701 (2008).
56. C. Tan, Z. Liu, J. Li, X. Guo, L. Wang, A. Sancar, D. Zhong, A. Ben-Shem, F. Frolow, N. Nelson, T. Brixner, R. Hildner, D. Brinks, J. B. Nieder, R. J. Cogdell, N. F. van Hulst, D. Polli, S. M. Harper, L. C. Neil, K. H. Gardner, A. R. Cashmore, J. A. Jarillo, Y. J. Wu, D. M. Liu, A. Sancar, D. Zhong, A. Sancar, A. Stuchebrukhov, D. Zhong, O. A. Sytina, Y.-T. Kao, C. Saxena, L. Wang, A. Sancar, D. Zhong, J. Li, Z. Liu, Z. Liu, D. E. Brash, L. Xu, H. W. Park, S. T. Kim, A. Sancar, J. Deisenhofer, A. Mees, C.-W. Chang, H. Y. Wang, A. A. Hassanali, D. Zhong, S. J. Singer, C. B. Harrison, L. L. O'Neil, O. Wiest, H. Sumi, R. A. Marcus, C. C. Page, C. C. Moser, X. X. Chen, P. L. Dutton, Z. Liu, Z. Liu, Y.-T. Kao, J. Hahn, M. E. Michel-Beyerle, N. Rosch, M. A. Huels, B. Boudaiffa, P. Cloutier, D. Hunting, L. Sanche, A. Sancar, F. W. Smith, G. B. Sancar, P. F. Heelis, G. Payne, A. Sancar, M. S. Jorns, G. B. Sancar, A. Sancar, S. T. Kim, A. Sancar, Y.-T. Kao, C. Saxena, A. Sancar, D. Zhong, The molecular origin of high DNA-repair efficiency by photolyase. *Nat. Commun.* **6**, 7302 (2015).
57. V. Thiagarajan, M. Byrdin, A. P. M. Eker, P. Müller, K. Brettel, Kinetics of cyclobutane thymine dimer splitting by DNA photolyase directly monitored in the UV. *Proc. Natl. Acad. Sci. U. S. A.* **108**, 9402–9407 (2011).
58. T. R. Prytkova, D. N. Beratan, S. S. Skourtis, Photoselected electron transfer pathways in DNA photolyase. *Proc. Natl. Acad. Sci. U. S. A.* **104**, 802–807 (2007).
59. Z. Liu, L. Wang, D. Zhong, Dynamics and mechanisms of DNA repair by photolyase. *Phys. Chem. Chem. Phys.* **17**, 11933–11949 (2015).
60. B. J. G. Rousseau, S. Shafei, A. Migliore, R. J. Stanley, D. N. Beratan, Determinants of Photolyase's DNA Repair Mechanism in Mesophiles and Extremophiles. *J. Am. Chem. Soc.* **140**, 2853–2861 (2018).
61. V. Thiagarajan, S. Villette, A. Espagne, A. P. Eker, K. Brettel, M. Byrdin, DNA repair by photolyase: a novel substrate with low background absorption around 265 nm for transient absorption studies in the UV. *Biochemistry*. **49**, 297–303 (2010).
62. K. Yang, R. J. Stanley, The Extent of DNA Deformation in DNA Photolyase– Substrate Complexes: A Solution State Fluorescence Study. *Photochem. Photobiol.* **84**, 741–749 (2008).
63. P. H. Harbach, M. Schneider, S. Faraji, A. Dreuw, Intermolecular Coulombic Decay in Biology: The Initial Electron Detachment from FADH–in DNA Photolyases. *J. Phys. Chem. Lett.* **4**, 943–949 (2013).
64. T. Gruhl, T. Weinert, M. J. Rodrigues, C. J. Milne, G. Ortolani, K. Nass, E. Nango, S. Sen, P. J. M. Johnson, C. Cirelli, A. Furrer, S. Mous, P. Skopintsev, D. James, F. Dworkowski, P. Båth, D. Kekilli, D. Ozerov, R. Tanaka, H. Glover, C. Bacellar, S. Brünle, C. M. Casadei, A. D. Diethelm, D. Gashi, G. Gotthard, R. Guixà-González, Y. Joti, V. Kabanova, G. Knopp, E. Lesca, P. Ma, I. Martiel, J. Mühle, S. Owada, F. Pamula, D. Sarabi, O. Tejero, C. J. Tsai, N. Varma, A. Wach, S. Boutet, K. Tono, P. Nogly, X. Deupi, S. Iwata, R. Neutze, J. Standfuss, G. Schertler, V. Panneels, Ultrafast structural changes direct the first molecular events of vision. *Nature*. **615**, 939–944 (2023).
65. K. Pande, C. D. M. Hutchison, G. Groenhof, A. Aquila, J. S. Robinson, J. Tenboer, S. Basu, S. Boutet, D. P. DePonte, M. Liang, T. A. White, N. A. Zatsepin, O. Yefanov, D. Morozov, D. Oberthuer, C. Gati, G. Subramanian, D. James, Y. Zhao, J. Koralek, J. Brayshaw, C. Kupitz, C. Conrad, S. Roy-Chowdhury, J. D. Coe, M. Metz, P. L. Xavier, T. D. Grant, J. E. Koglin, G. Ketawala, R. Fromme, V. Šrajer, R. Henning, J. C. H. Spence, A. Ourmazd, P. Schwander, U. Weierstall, M. Frank, P. Fromme, A. Barty, H. N. Chapman, K. Moffat, J. J. van Thor, M. Schmidt, Femtosecond structural dynamics drives the trans/cis isomerization in photoactive yellow protein. *Science*. **352**, 725–729 (2016).
66. A. D. McNaught, A. Wilkinson, *IUPAC. Compendium of Chemical Terminology (the "Gold Book")* (Blackwell Scientific Publications, Oxford, 2nd ed., 1997; https://doi.org/10.1351/goldbook).
67. C.-Y. Chen, Y.-C. Chang, B.-L. Lin, C.-H. Huang, M.-D. Tsai, Temperature-Resolved Cryo-EM Uncovers Structural Bases of Temperature-Dependent Enzyme Functions. *J. Am. Chem. Soc.* **141**, 19983–19987 (2019).
68. M. Sugahara, E. Mizohata, E. Nango, M. Suzuki, T. Tanaka, T. Masuda, R. Tanaka, T. Shimamura, Y. Tanaka, C. Suno, K. Ihara, D. Pan, K. Kakinouchi, S. Sugiyama, M. Murata, T. Inoue, K. Tono, C.

Song, J. Park, T. Kameshima, T. Hatsui, Y. Joti, M. Yabashi, S. Iwata, Grease matrix as a versatile carrier of proteins for serial crystallography. *Nat. Methods*. **12**, 61–63 (2014).
69. T. Ishikawa, H. Aoyagi, T. Asaka, Y. Asano, N. Azumi, T. Bizen, H. Ego, K. Fukami, T. Fukui, Y. Furukawa, S. Goto, H. Hanaki, T. Hara, T. Hasegawa, T. Hatsui, A. Higashiya, T. Hirono, N. Hosoda, M. Ishii, T. Inagaki, Y. Inubushi, T. Itoga, Y. Joti, M. Kago, T. Kameshima, H. Kimura, Y. Kirihara, A. Kiyomichi, T. Kobayashi, C. Kondo, T. Kudo, H. Maesaka, X. M. Maréchal, T. Masuda, S. Matsubara, T. Matsumoto, T. Matsushita, S. Matsui, M. Nagasono, N. Nariyama, H. Ohashi, T. Ohata, T. Ohshima, S. Ono, Y. Otake, C. Saji, T. Sakurai, T. Sato, K. Sawada, T. Seike, K. Shirasawa, T. Sugimoto, S. Suzuki, S. Takahashi, H. Takebe, K. Takeshita, K. Tamasaku, H. Tanaka, R. Tanaka, T. Tanaka, T. Togashi, K. Togawa, A. Tokuhisa, H. Tomizawa, K. Tono, S. Wu, M. Yabashi, M. Yamaga, A. Yamashita, K. Yanagida, C. Zhang, T. Shintake, H. Kitamura, N. Kumagai, A compact X-ray free-electron laser emitting in the sub-ångström region. *Nat. Photonics*. **6**, 540–544 (2012).
70. K. Tono, E. Nango, M. Sugahara, C. Song, J. Park, T. Tanaka, R. Tanaka, Y. Joti, T. Kameshima, S. Ono, T. Hatsui, E. Mizohata, M. Suzuki, T. Shimamura, Y. Tanaka, S. Iwata, M. Yabashi, Diverse application platform for hard X-ray diffraction in SACLA (DAPHNIS): Application to serial protein crystallography using an X-ray free-electron laser. *J. Synchrotron Radiat.* **22**, 532–537 (2015).
71. Y. Shimazu, K. Tono, T. Tanaka, Y. Yamanaka, T. Nakane, C. Mori, K. T. Kimura, T. Fujiwara, M. Sugahara, R. Tanaka, R. B. Doak, T. Shimamura, S. Iwata, E. Nango, M. Yabashi, High-viscosity sample-injection device for serial femtosecond crystallography at atmospheric pressure. *J. Appl. Crystallogr.* **52**, 1280–1288 (2019).
72. T. Kameshima, S. Ono, T. Kudo, K. Ozaki, Y. Kirihara, K. Kobayashi, Y. Inubushi, M. Yabashi, T. Horigome, A. Holland, K. Holland, D. Burt, H. Murao, T. Hatsui, Development of an X-ray pixel detector with multi-port charge-coupled device for X-ray free-electron laser experiments. *Rev. Sci. Instrum.* **85**, 033110 (2014).
73. T. Nakane, Y. Joti, K. Tono, M. Yabashi, E. Nango, S. Iwata, R. Ishitani, O. Nureki, Data processing pipeline for serial femtosecond crystallography at SACLA. *J. Appl. Crystallogr.* **49**, 1035–1041 (2016).
74. E. Prat, R. Abela, M. Aiba, A. Alarcon, J. Alex, Y. Arbelo, C. Arrell, V. Arsov, C. Bacellar, C. Beard, P. Beaud, S. Bettoni, R. Biffiger, M. Bopp, H. H. Braun, M. Calvi, A. Cassar, T. Celcer, M. Chergui, P. Chevtsov, C. Cirelli, A. Citterio, P. Craievich, M. C. Divall, A. Dax, M. Dehler, Y. Deng, A. Dietrich, P. Dijkstal, R. Dinapoli, S. Dordevic, S. Ebner, D. Engeler, C. Erny, V. Esposito, E. Ferrari, U. Flechsig, R. Follath, F. Frei, R. Ganter, T. Garvey, Z. Geng, A. Gobbo, C. Gough, A. Hauff, C. P. Hauri, N. Hiller, S. Hunziker, M. Huppert, G. Ingold, R. Ischebeck, M. Janousch, P. J. M. Johnson, S. L. Johnson, P. Juranić, M. Jurcevic, M. Kaiser, R. Kalt, B. Keil, D. Kiselev, C. Kittel, G. Knopp, W. Koprek, M. Laznovsky, H. T. Lemke, D. L. Sancho, F. Löhl, A. Malyzhenkov, G. F. Mancini, R. Mankowsky, F. Marcellini, G. Marinkovic, I. Martiel, F. Märki, C. J. Milne, A. Mozzanica, K. Nass, G. L. Orlandi, C. O. Loch, M. Paraliev, B. Patterson, L. Patthey, B. Pedrini, M. Pedrozzi, C. Pradervand, P. Radi, J. Y. Raguin, S. Redford, J. Rehanek, S. Reiche, L. Rivkin, A. Romann, L. Sala, M. Sander, T. Schietinger, T. Schilcher, V. Schlott, T. Schmidt, M. Seidel, M. Stadler, L. Stingelin, C. Svetina, D. M. Treyer, A. Trisorio, C. Vicario, D. Voulot, A. Wrulich, S. Zerdane, E. Zimoch, A compact and cost-effective hard X-ray free-electron laser driven by a high-brightness and low-energy electron beam. *Nat. Photonics*. **14**, 748–754 (2020).
75. T. A. White, Processing serial crystallography data with crystFEL: A step-by-step guide. *Acta Crystallogr. Sect. D Struct. Biol.* **75**, 219–233 (2019).
76. T. A. White, R. A. Kirian, A. V. Martin, A. Aquila, K. Nass, A. Barty, H. N. Chapman, CrystFEL: A software suite for snapshot serial crystallography. *J. Appl. Crystallogr.* **45**, 335–341 (2012).

Author Contributions

MMR, AR, JY, SI, JS, YB, LOE, and MDT conceived the research and designed experiments. MMR, PHW, EN, YH, MS, AF, CHY, EPGNP, WJW, HJE, SF-B, CY, SE, NC, MW, HLG, TW, HYW, CCL, WCH, KFH, YKC, JHL, JHW, WG, CWC, AHP, KCY, WTL, YCC, DG, EB, GK, CC, CM, CB, MS, YJ, AY, RT, TT, FL, KT, MAA, FB, VF, PG, SK, LK, VR, CJR, EMS, MW, LW, RS, AR, JY, YB, and LOE performed experiments. MMR, DO, KN, RS, AR, and LOE were responsible for on-site data processing at SwissFEL, MMR, CHY, YJ, RS, AR, and LOE fulfilled the same role at SACLA. PJMJ was responsible for pump laser setup at SwissFEL, while SO at SACLA. MMR, PHW, EN, CHY, SK, RS, AR, JY, YB, LOE and MDT analyzed the data. MMR, PHW, EPGNP, LOE, and AR performed *in crystallo* spectroscopy. PHW performed in-solution spectroscopy. WZ and PM determined quantum yield spectroscopically. NC and AR performed SVD analyses. CHY performed QM calculation. MMR, PHW and CHY established and analyzed the refinement protocol. DZ provided critical insight on the early events of dimer repair. MMR, CHY, LOE, and MDT wrote the manuscript.

Competing Interests

The authors declare no conflict of financial interest.

ACKNOWLEDGMENTS

The work was supported by Academia Sinica and the Taiwan Protein Project funded by Ministry of Science and Technology (Grant No. AS-KPQ-105-TPP and AS-KPQ-109-TPP2 to MDT), and in part by JSPS KAKENHI (16K01942) to YB, by Air Force Office of Scientific Research (AFOSR; Grant No. FA9550-14-1-0409) and German Research Foundation (DFG, Grant No. ES152/18) to LOE, by the National Science and Technology Council (NSTC, 111-2113-M-002-029-MY3) to MMR, by the Ministry of Education, Culture, Sports, Science and Technology of Japan (Grants-in-Aid for Scientific Research on Innovative Areas “Molecular movie”, JP20H05442) and JST FOREST (JPMJFR2057) to JY, by Platform Project for Supporting Drug Discovery and Life Science Research (Basis for Supporting Innovative Drug Discovery and Life Science Research (BINDS) from Japan Agency for Medical Research and Development (AMED) to SI and EN, and by JSPS KAKENHI Grant Numbers JP19H05776 (to SI). The XFEL experiments were performed at the BL2 of SACLA with the approval of the Japan Synchrotron Radiation Research Institute (JASRI) (Proposal No. 2017A8019, 2017B8052, 2018A8008,

2018B8031, 2019A8014, 2019B8005). SwissFEL experiments were performed at the ALVRA beamline (Proposal No. 20191801 and 20190089). This work used the *ic*OS platform of the Grenoble Instruct-ERIC center (ISBG; UAR 3518 CNRS-CEA-UGA-EMBL) within the Grenoble Partnership for Structural Biology (PSB), supported by FRISBI (ANR-10-INBS-0005-02) and GRAL, financed within the University Grenoble Alpes graduate school (Ecoles Universitaires de Recherche) CBH-EUR-GS (ANR-17-EURE-0003). We thank Toshi Arima, Yoshinori Matsuura, Hisashi Naitow, Naoki Kunishima, Makoto Nishiyama, Tetsukon Kin, and the members of Engineering Support Team of SACLA for help during our X-ray experiments, as well as to Takanori Nakane for his introduction to CrystFEL. We thank all staff members of the TPS05A beamline, NSRRC, a national user facility supported by MOST, ROC, and in particular Chien-Chang Tseng and Chung-Kuang Chou for their help in setting up non-standard conditions for crystal testing. We would also like to thank all staff members of the BL32XU beamline, SPring-8, Japan, for their help in setting up SACLA-similar beam conditions for testing our crystals prior to SACLA beamtime. Also, Hui-Lin Shr (Crystallization Facility of the Institute of Biological Chemistry, Academia Sinica) provided the facility for crystallization under non-standard conditions, which were initially tested with equipment kindly provided by Dr. Shin-Guang Shyu. The graphics for the summary figure was illustrated by Ying Wang; we thank Julian C. Essen for delicate transport of crystals and logistic support at the SwissFEL site. Finally, we thank Prof. Gebhard Schertler for very stimulating discussion on the analytical value of quantifying negative electron density within difference density maps. MD Tsai wishes to dedicate this work to his former Ph.D. advisor Prof. Heinz G. Floss, 1934-2022, and LO Essen wishes to dedicate this work to his former mentor Prof. Dieter Oesterhelt, 1940-2022.

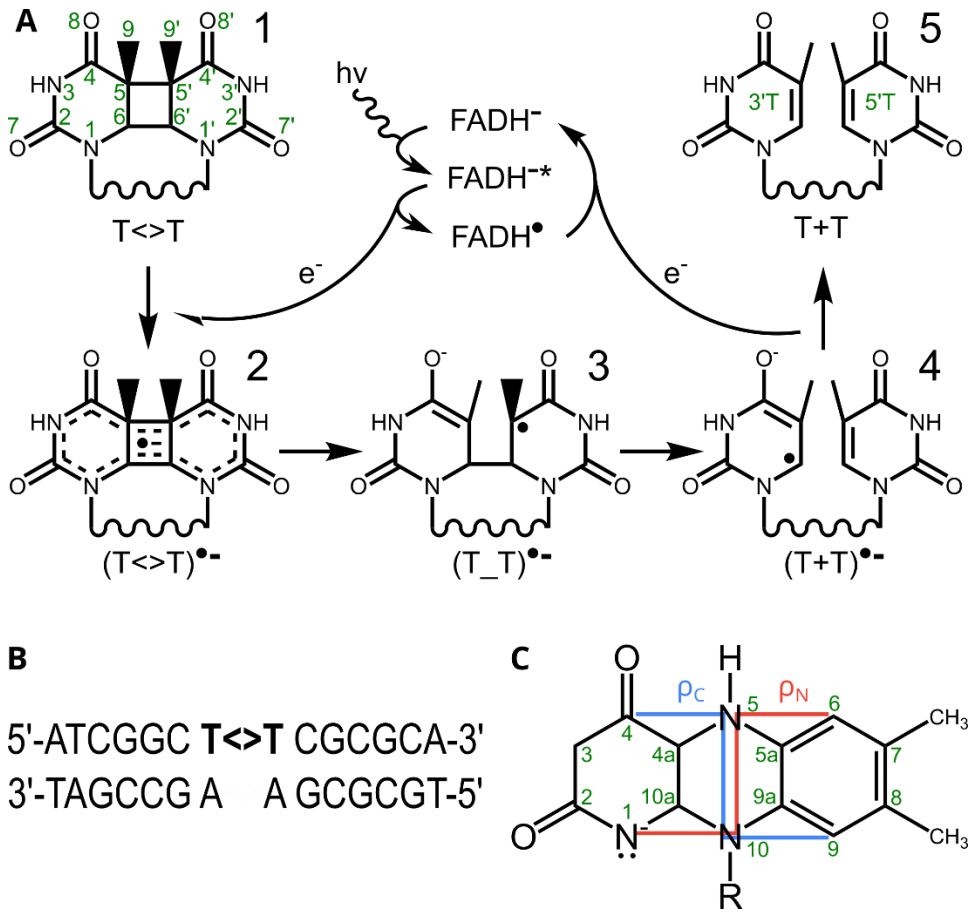

Fig. 1. Proposed intermediates during repair of T<>T lesions as catalyzed by DNA photolyases. (**A**) Canonical scheme of DNA repair by CPD-photolyases. (**B**) The CPD-lesion comprising dsDNA used in this work, which contained the *cis-syn* CPD with its phosphodiester linkage (*43*). (**C**) Illustration of the ρ_C and ρ_N dihedral angles of the $FADH^-$ isoalloxazine moiety. As shown by TR-SFX of photoreduction, the isoalloxazine moiety of FAD in *Mm*CPDII undergoes symmetrical buckling or bending ($\rho_C = \rho_N$) or asymmetrical twisting ($\rho_C \neq \rho_N$) upon redox change (*33*). Most importantly, the transition from one geometry to another is orders of magnitude slower than electron transfer itself.

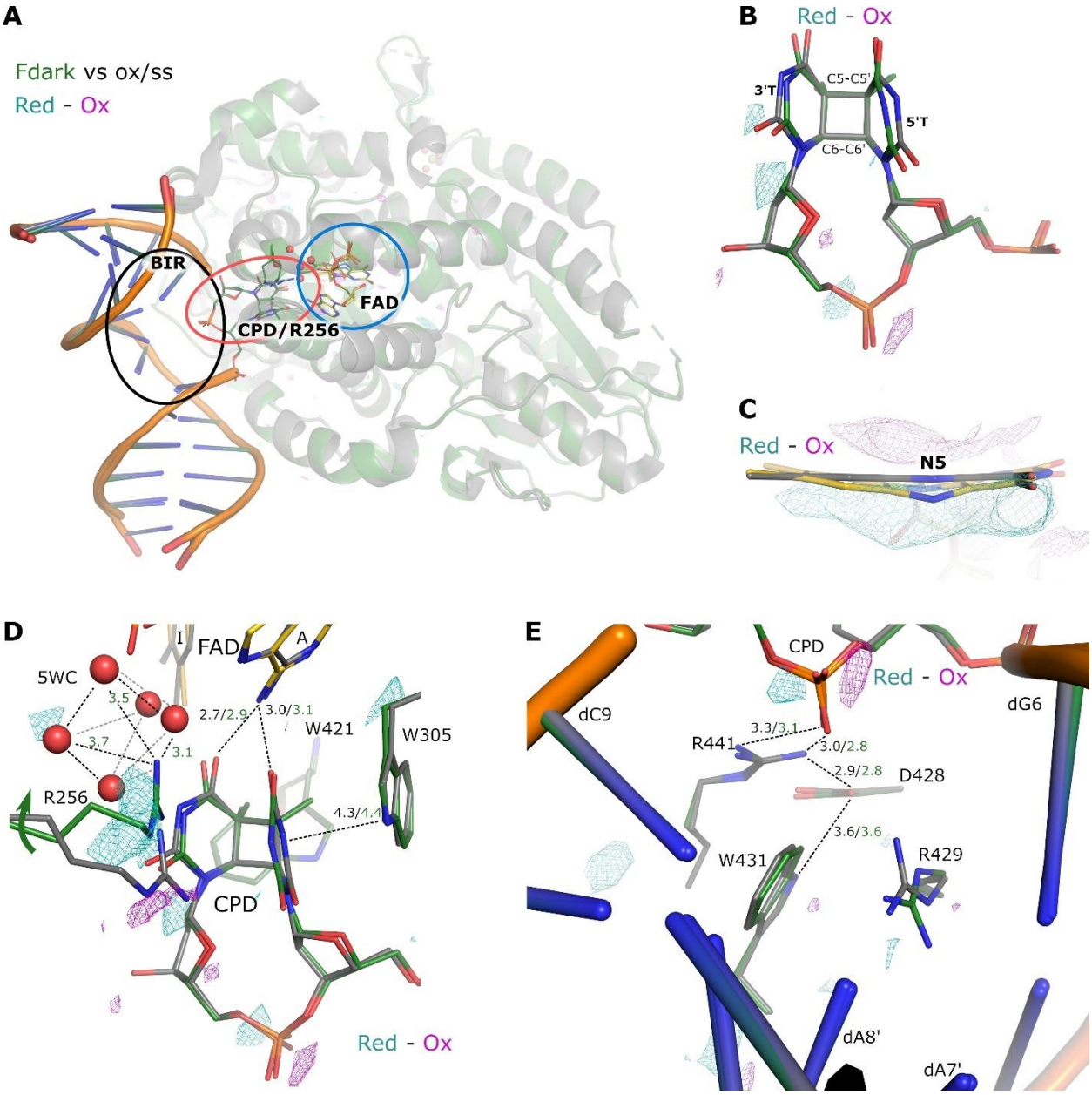

Fig. 2. Static structures of *Mm*CPDII complexes with damaged DNA and illustration of the four main reaction loci. Structure of Fdark (reduced, green) superposed with ox/ss (steady state oxidized, gray) are shown along with 3σ-contoured difference maps between the dark and oxidized states, ΔFo(dark-ox/ss) (positive peaks in cyan, negative peaks in magenta). (**A**) Global structures showing the overall fold, with the bound DNA backbone in orange. (**B**) Structures of the bound CPD. (**C**) Structures of the isoalloxazine ring in the oxidized (FAD_{ox}, gray) and fully reduced form ($FADH^-$, gold), showing increased buckling of the FAD in the reduced state. (**D**) The 5WC/R256 locus at the active site. The interactions between CPD, FAD and active site residues R256, W305, and W421, and the five-water cluster (5WC) that only appears in the Fdark state are also shown. In the presence of the 5WC, R256 undergoes a conformational change, with its guanidinium moiety becoming the final vertex in the bipyramidal 5WC. Some interatomic distances are highlighted by dashed lines with values in Ångstrom nearby. (**E**) The bubble-intruding region (BIR)

with its D428/W431/R441 locking triad, as well as R429, which mostly interacts with the unpaired bases dA7’ and dA8’ complementary to the thymine dimer. The lack of significant difference electron density here suggests little conformational change related to the flavin’s redox state for this region.

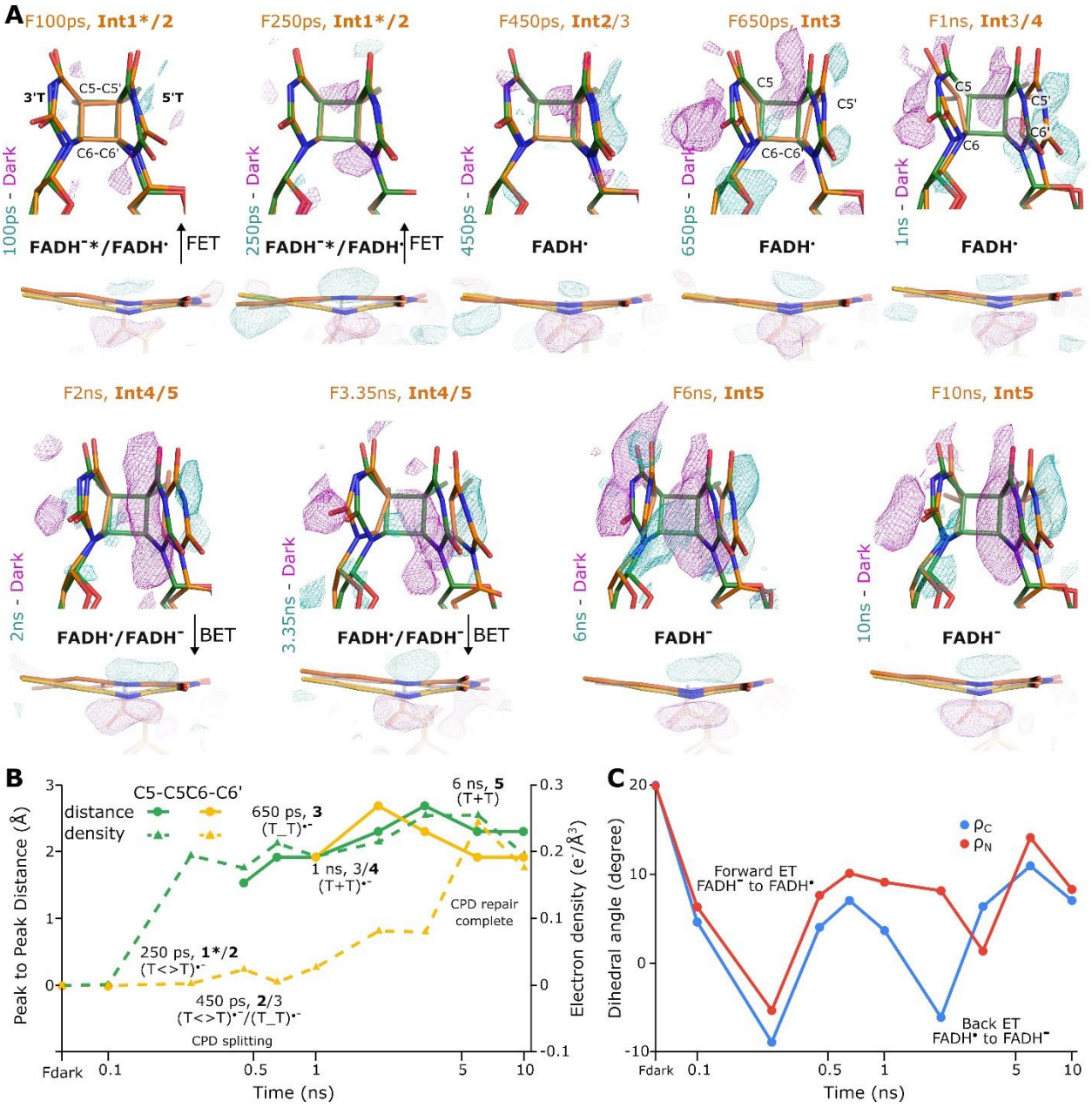

Fig. 3. **Bond breaking and ring opening during cleavage of the cyclobutane ring.** (**A**) Structures of the CPD moiety (T<>T) of the bound DNA as well as the FAD isoalloxazine moiety from the first TR-SFX series (orange), from F100ps to F10ns, each superposed with the reduced dark structure (Fdark in green and $FADH^-$ in gold). Each panel also shows 3σ-contoured ΔFo(Y-dark) maps, with positive peaks in cyan and negative ones in magenta. (**B**) Plots of C5-C5' (green) and C6-C6' (orange) peak distances (full lines) and average integrated negative electron densities (dashed lines) over time. Since both the negative cyclobutane and the positive 5'-T peaks are necessary to calculate peak distances, when either is missing, the distance could not be calculated and no value is plotted (100 to 250 ps for C5-C5' and 100 ps to 650 ps for C6-C6'). (**C**) Plots of ρ_C (blue) and ρ_N (red) dihedral angles over time.

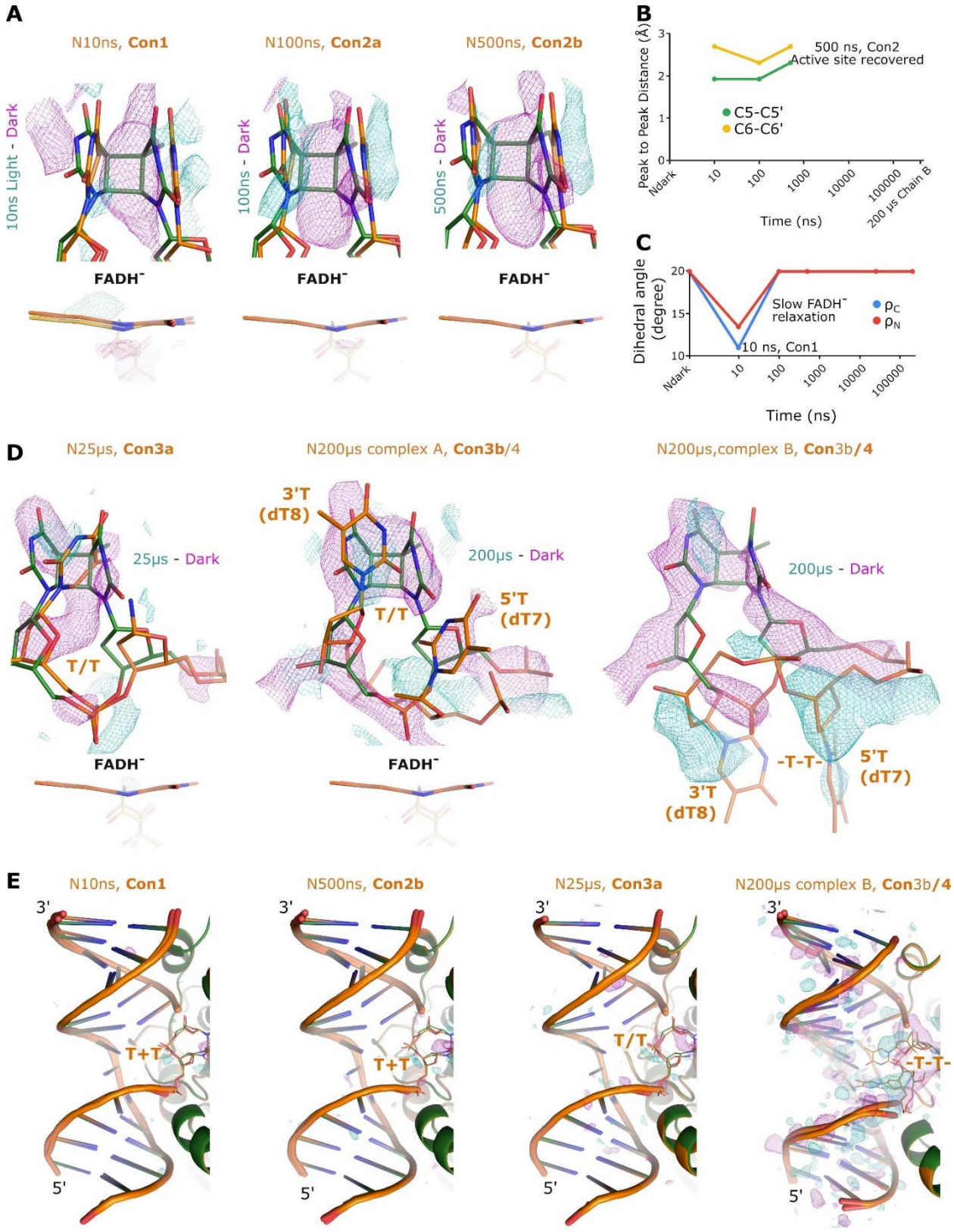

Fig. 4. Post-repair events leading to thymine base return and DNA release. (**A**) Structures of the newly repaired thymines (T||T) as well as the isoalloxazine moiety from the second TR-SFX series (orange), from

N10ns, N100ns, and N500ns, each superposed over the reduced dark structure (Ndark CPD shown in green, while its isoalloxazine moiety is depicted in gold). Each panel also shows 3σ-contoured ΔFo(Y-dark) maps, with positive peaks in cyan and negative ones in magenta. (**B**) Peak distance plots along the C5-C5' (green) and C6-C6' (yellow) axes, and (**C**) ρ_C (blue) and ρ_N (red) angles plots over time for the second TR-SFX time-series. (**D**) Structures of the newly repaired thymines from the second TR-SFX series (orange) during their return to the dsDNA, including N25μs and N200μs, each superposed over the reduced dark structure (Ndark in green). Because the two *Mm*CPDII-DNA complexes in N200μs are at two different DNA release stages, they are both shown here. Each panel also shows 3σ-contoured ΔFo(Y-dark) maps as in (A). (**E)** Difference maps at the dsDNA, from left to right: N10ns, N500ns, N25μs and complex B from N200μs. For all complexes, 3σ contoured ΔFo(Y-dark) maps are superposed over the entire DNA molecule.

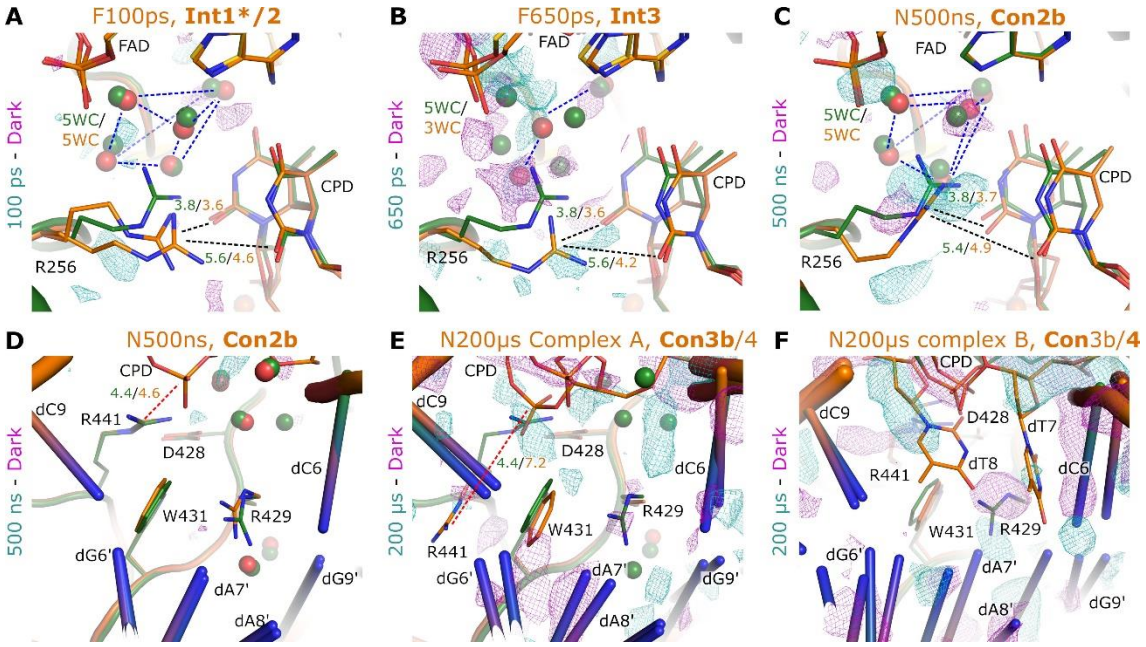

Fig. 5. Roles of the 5WC/R256 locus during DNA repair and the BIR locus during DNA release. (A-C) Detailed structures of the 5WC/R256 locus (orange, F100ps for A, F650ps for B and N500ns for C) superposed with the corresponding dark structure (green). The FAD coenzyme is depicted in gold for both structures in each panel. The R256 side chain is dynamic with two alternative conformations at 100 ps. 3σ contoured ΔFo(Y-dark) maps are shown as well, with positive peaks in cyan, and negative ones in magenta. The characteristic dark five-water cluster (5WC) is shown as green spheres, while the remaining water molecules for each specific time-resolved snapshot in red. Here, blue dotted lines highlight the 5WC arrangement in each time-resolved snapshot. Notably, already at 100 ps (A), the square bipyramidal interaction between 5WC and R256 is broken, resulting in a square pyramidal arrangement. R256 and the CPD are shown as stick figures, with interatomic distances between the center of mass of the R256 guanidinium moiety and the O2 carbonyl of each of the CPD thymines highlighted with black dotted lines. Distances in Ångstrom are provided nearby and are color-coded as the structures themselves. (**D-F)** Detailed view of the unpaired bubble and the BIR residues D428, R429, W431 and R441 with Ndark (green) superposed onto three individual time-resolved snapshots (D: N500ns, E: N200µs complex A, F: N200µs complex B). dT7 and dT8, corresponding to the CPD bases, as well as all BIR residues are shown as stick models, while all other bases and amino acids as cartoon representations. 3σ contoured ΔFo(Y-dark) maps as above are shown as well. To highlight BIR lock opening, marked by the movement of R441, the R441 to CPD phosphate center of mass distance is shown as a red dashed line, with color-coded distances in Ångstrom provided nearby.

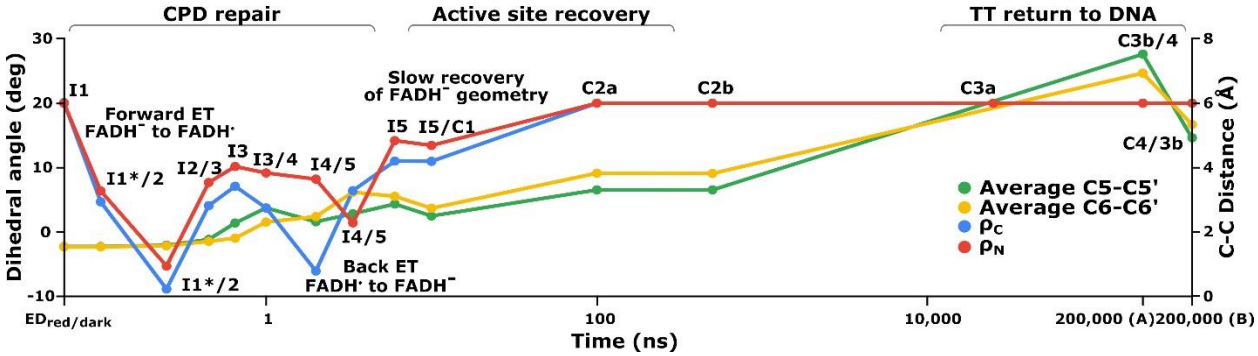

Fig. 6. The complete timeline for major events and video presentation. Evolution of the average C5-C5'and C6-C6' atomic distances of the CPD, and dihedral angles of the isoalloxazine ring of FAD, as derived from our structural models. The intermediate number(s) for each time point, and the catalytic hallmarks of different time periods, are indicated. The intermediates up to 10 ns are reaction intermediates for CPD repair (**Int1 to Int5**), while the intermediates from 10 ns upward are conformational intermediates (**Con1 to Con4**) in the processes of active site recovery and product release. Importantly, since the refined structural models may represent an average structure derived from the composite of different intermediates present at any given time-point, the evolving C5-C5' and C6-C6' distances should not be simply considered as bond elongation, but rather, as shifts in the populations of bond split/unsplit intermediates. In any case, these values visualize the progress along the reaction coordinate for CPD cleavage over time.

Movie 1: A molecular movie showing the key structural components of all intermediates highlighted in Fig. 6.

https://vimeo.com/802945501/90b53c6781

Table 1. Properties of the static and time-resolved structures of *Mm*CPDII complexes with damaged DNA.

1	2	3	4	5	6	7	8	9	10	11
Structure[a]	Interm.[a]	TT state	FAD state	ρ_{C} / ρ_{N} (deg)	5WC /R256[f]	BIR[g] D428/W431/ R441	CC peak distance C5/C6 (Å)[c]	Negative densities C5/C6 (e^{-}/Å^3)[e]	PDB code	Resol (Å)
Oxidized photolyase:DNA complex										
ox/ss		T<>T	FAD_{ox}	2.0/2.1	Dynamic /CPD[f]	Locked	-/-	0 / 0	7YE0	2.75
ps-ns time series (SwissFEL)										
Fdark	**Int1**	T<>T	$FADH^{-}$	20.1/20.0	Ordered /5WC	Locked	-/-	0 / 0	7YC7	1.95
F100ps	**Int1*/2**	FET[b] T<>T / $(T<>T)^{\bullet-}$	FET[b] $FADH^{-}$* /$FADH^{\bullet}$	4.6/6.3	Ordered /CPD		-/-	0.00/0.00	7YCM	2.00
F250ps	**Int1*/2**			-8.9/-5.3	Dynamic /CPD		-/-	0.19/0.00	7YCP	2.08
F450ps	**Int2**/3	$(T<>T)^{\bullet-}$	$FADH^{\bullet}$	4.0/7.6			1.5/-	0.18/0.02	7YCR	2.15
F650ps	**Int3**	$(T\_T)^{\bullet-}$		7.1/10.1			1.9/-	0.21/0.03	7YD6	2.15
F1ns	Int3/**4**	$(T+T)^{\bullet-}$		3.7/9.1			1.9/1.9	0.19/0.03	7YD7	2.25
F2ns	**Int4/5**	BET[b] $(T+T)^{\bullet-}$ /T+T	$FADH^{\bullet}$ /$FADH^{-}$	-6.1/8.2			2.3/2.7	0.21/0.08	7YD8	2.15
F3.35ns				6.4/1.4			2.7/2.3	0.25/0.08	7YEB	2.20
F6ns	**Int5**	T+T	$FADH^{-}$ recovering	11.0/14.2			2.3/1.9	0.25/0.24	7YEC	2.20
F10ns				7.1/8.3			2.3/1.9	0.19/0.18	7YEE	2.15
ns-µs series (SACLA)										
Ndark		T<>T	$FADH^{-}$	20.0/20.0	Ordered /5WC	Locked	-/-	n.d./n.d.	7YDZ	2.23
N10ns	**Con1**	T+T	$FADH^{-}$ recovering	10.9/13.4	Dynamic /CPD		1.9/1.9		7YEI	2.70
N100ns	**Con2a**	T+T	$FADH^{-}$ recovered	20.0/20.0	Dynami /5WC		1.9/2.3		7YEJ	2.55
N500ns	**Con2b**				Ordered /5WC		2.3/2.7		7YEK	2.40
N25µs	**Con3a**	T/T				Unlocking	-/-[d]		7YEL	2.55
N200µsA[a]	**Con 3b/4**	T/T			N/A[f]		-/-[d]		7YEM	2.60
N200µsB[a]	**Con 4**/3b	-T-T-				Unlocked	-/-[d]		7YEM	2.60

[a]The definitions of structure names and intermediate numbers are explained in the text. Each structure has a PDB code, except that N200µsA and N200µsB share the same PDB code (7YEM) since they correspond in N200µs to the two independent complexes, A and B, of the asymmetric unit. When multiple

intermediates coexist in a structure, the bolded number designates the major form. F250ps may also contain a contribution by Int3 based on negative density at C5-C5' only.

[b]FET and BET designate forward electron transfer and back electron transfer, respectively. Here, no dominant CPD, TT and FAD intermediates can be defined. These structures should be hence considered as mixtures.

[c]C-C peak distances corresponding to the distance between the maxima of the characteristic CPD repair signals, i.e. the cyclobutane negative density and the 5'-T positive density, along the C5-C5' and the C6-C6' axes. The position of the maximum was calculated as described in **Materials and methods summary** and **fig. S5**.

[d]The thymine bases have started to flip back to pair with adenine bases.

[e]The average integrated negative electron densities from difference maps around C5 and C6 atoms calculated as described in **Supplementary Text S4, fig. S13B**.

[f]The conformations of active site moieties 5WC and R256 sidechain. 5WC is designated as ordered (intact) or dynamic. R256 is designated as pointing toward 5WC or CPD. N/A for 200 μs because the thymine bases have moved out of the active site.

[g]BIR: The bubble intruding region composed of amino-acids D428, W431, and R441 acts as a lock. In its locked state, BIR stabilizes the unpaired bubble and prevents CPD flip-back before repair. Upon completion of CPD repair, flip-back of the repaired bases unlocks BIR, displaces it and initiates product release.